Astronomy & Astrophysics manuscript no. output
June 27, 2025

Spatially Resolved Star Formation relations in local LIRGs along the complete merger sequence

M. Sánchez-García[1,2], T. Díaz-Santos[1,2], L. Barcos-Muñoz[3,4], A. S. Evans[3,4], Y. Song[5,6], M. Pereira-Santaella[7], S. García-Burillo[8], S. T. Linden[9], C. Ricci[10], L. Lenkic[11], A. Zanella[12], L. Armus[11], C. Eibensteiner[3], Y.-H. Teng[13], A. Saravia[4], V. A. Buiten[14], G. C. Privon[3,4,15], N. Torres-Albà[4], T. Saito[16], K. L. Larson[17], M. Bianchin[18], A. M. Medling[19], T. Lai[20], G. P. Donnelly[21], V. Charmandaris[1,2], T. Bohn[22], C. M. Lofaro[1,2], and G. Meza[23]

(Affiliations can be found after the references)

June 27, 2025

ABSTRACT

We investigate the properties of the interstellar medium (ISM) at giant molecular cloud (GMC) scales (< 100 pc) in a sample of 27 nearby luminous infrared galaxies (LIRGs) spanning all interacting stages along the merger sequence; i.e., from isolated systems to late-stage mergers. In particular, we study the relations between star-formation (SF) and molecular gas surface density as a function of the interaction stage by (1) defining beam-sized (unresolved, line-of-sight) regions and (2) identifying actual gas clumps and physical structures within the galaxies. In total, we identify more than 4000 beam-sized CO-emitting regions defined on scales of 90 pc and more than 1000 molecular gas clumps in the sample. To map the distribution of molecular gas we use ALMA to observe the J = 2–1 CO transition, and to map the distribution of star formation we use HST observations of the Paα or Paβ hydrogen recombination lines. We derive spatially resolved Kennicutt–Schmidt (KS) relations for each LIRG in the sample. When using beam-sized regions, we find that 67% of galaxies follow a single relation between Σ_{SFR} and Σ_{H2}. However, in the remaining galaxies, the relation splits into two branches – one is characterised by higher Σ_{SFR} and Σ_{H2}, while the other exhibits lower values – indicating a duality similar to that identified by Sánchez-García et al. (2022a). In contrast, when using physical gas clumps, the duality disappears and all galaxies show a single trend. These results provide two complementary perspectives when studying the star formation process: one that maximises the number statistics (beam-sized regions), and another that focuses on actual structures associated to gas clumps in which the measured sizes have a physical meaning. We also study other ISM/clump properties as a function of the merger stage of the LIRG systems. We find that isolated galaxies and systems in early stages of interaction exhibit lower amounts of gas and star formation. As the merger progresses, however, the amount of gas in the central kiloparsecs of the galaxy undergoing the merger increases, along with the SFR, and the slope of the KS relation becomes steeper, indicating an increase in the SF efficiency of the molecular gas clumps. Clumps in late-stage mergers are predominantly located at small distances from the nucleus, confirming that most of the activity is concentrated in the central regions. Most interestingly, the relation between the gas depletion time scale and the boundedness parameter (which measures the effects of gravity against velocity dispersion) changes from roughly flat at early merger stages to negative for the two last merger phases, implying that more bounded clumps are forming stars at a higher rate in the final stages of the interaction.

Key words. galaxies: star formation – infrared: galaxies – galaxies: ISM – ISM: clouds

1. Introduction

Star formation (SF) takes place primarily within structures of molecular gas, called Giant Molecular Clouds (GMCs). Stellar feedback —in the form of stellar winds, supernova explosions, and radiation pressure from massive stars— plays a significant role in the formation, evolution, and lifetimes of molecular clouds (e.g. Schinnerer & Leroy 2024). These processes inject energy and momentum into the interstellar medium (ISM), creating turbulence and disrupting the equilibrium of the gas. The compression and turbulence induced by stellar feedback, as well as the shear induced by galactic dynamics (Chevance et al. 2020), can trigger the collapse of molecular clouds, initiating the formation of new stars. However, stellar feedback can also lead to the destruction of molecular clouds (e.g. Bonne et al. 2023). Chevance et al. (2022) suggested that the main causes of cloud destruction in galaxies are early stellar feedback mechanisms. It is still a matter of debate as to whether SF is more influenced by the environment —for example, central regions versus spiral arms— or by stellar feedback mechanisms (Corbelli et al. 2017; Rey-Raposo et al. 2017; Kruijssen & Longmore 2014; Chevance et al. 2022; Liu et al. 2022; Choi et al. 2023).

The low-J CO transitions have been used for decades as the primary tracers of molecular gas in galaxies. In early CO studies on galaxies, the low spatial resolution of millimetre telescopes hindered the ability to resolve individual GMCs, and they were observed as unresolved complexes of CO emission above kiloparsec scales. These early CO images did not resolve the star formation process in GMCs. The large–kpc scale relationship between the rate at which stars form and the amount of gas contained in galaxies is commonly referred to as the star formation law or the Kennicutt-Schmidt (KS) relation (Schmidt 1959; Kennicutt 1998). Despite its success as an empirical law, the physical mechanisms that govern star formation remain unknown. Resolving molecular gas clouds to analyse their physical properties in different (large- and small-scale) environments within galaxies and linking this emission to that of young stars is crucial for understanding the ubiquity and genesis of the KS relation, as well as the variations in star formation efficiency across different galaxies and galaxy types.

Observations of molecular clouds in our Galaxy and in a number of nearby galaxies have identified various empirical trends manifesting such cloud–environment correlations. Within a galaxy, molecular clouds located closer to the galaxy centre

appear denser, more massive, and more turbulent (e.g. Oka et al. 2001; Colombo et al. 2014; Freeman et al. 2017; Hirota et al. 2018; Brunetti et al. 2021, also see Heyer & Dame 2015). Similar trends have been found in galaxy-scale numerical simulations (e.g. Jeffreson et al. 2020). Recent observational works also report that more massive and actively star-forming galaxies tend to host clouds with typically larger sizes, masses, surface densities, and velocity dispersions (Leroy et al. 2015, 2016; Schruba et al. 2019; Sun et al. 2020, see also Bolatto et al. 2008; Fukui & Kawamura 2010. However, galaxy mergers, which represent a crucial phase in galaxy evolution, have been scarcely studied, particularly in relation to GMCs. These events play a central role in shaping the growth, star formation history, and overall evolution of galaxies, influencing their dynamics and structure throughout the history of the universe.

To have a more concrete understanding of the mechanisms involved in the star formation process, we need to study the correlations between molecular clouds and their (sub-)galactic environment. In the molecular cloud literature, the characterization of environmental dependence is often qualitative, with environments typically defined in broad categorical terms—such as centers, stellar bars, and spiral arms—rather than through quantitative metrics. As a result, environmental factors are generally treated as secondary influences rather than systematically parameterized. To better understand the underlying physics, a more direct approach would be to quantify the dependence of molecular cloud properties on a set of quantitative "environmental metrics," such as the local gas and stellar mass surface density, and the star formation rate (SFR) surface density (e.g. Schruba et al. 2019).

Previous studies had to rely on observations of a small number of galaxies or subgalactic regions, which restricted the range of host galaxy properties that could be examined. While these studies provided unique insights for specific targets, only systematic large samples of galaxies can cover a wide range of host galaxy properties, produce representative population statistics, and establish meaningful connections with galaxy evolution models. This shift toward large-number statistics occurred with the PHANGS survey, which focused on star-forming main-sequence galaxies and enabled systematic investigations (Sun et al. 2018, 2022; Utomo et al. 2018; Leroy et al. 2021; Pessa et al. 2021; Kim et al. 2022). However, the more intense local starburst galaxies (i.e., luminous and ultraluminous infrared galaxies, LIRGs and ULIRGs) have not yet been studied in a substantial sample in the local Universe at GMC scales.

Multi-wavelength observations have shown that local LIRGs are a mixture of single disk galaxies, interacting systems, and advanced mergers, exhibiting enhanced SFRs and active galactic nucleus (AGN) activity compared to less luminous and non-interacting galaxies (c.f. Sanders & Mirabel 1996; Stierwalt et al. 2013; Larson et al. 2016). These extreme galaxies are important to consider in the context of the KS law (extreme starburst environments triggered by galaxy mergers in the local universe) which at low and high spatial resolutions have shown different behaviours from normal star-forming galaxies (e.g. Daddi et al. 2010; Genzel et al. 2010; García-Burillo et al. 2012; Sánchez-García et al. 2022a; Sánchez-García et al. 2022b; Saravia et al. 2025). U/LIRGs also provide an opportunity to investigate the impact of galaxy mergers on star formation, as well as their broader role in galaxy formation and evolution (e.g. Hopkins et al. 2006).

Since LIRGs are inherently dusty, it is crucial to study star formation in these systems in the infrared, where obscuration is minimized while maintaining high spatial resolution. In star-forming galaxies, hydrogen recombination emission lines are commonly used as SFR tracers, as their fluxes provide a direct measure of the number of ionizing photons emitted by massive O/B stars. However, the central kiloparsec of LIRGs is often heavily obscured and can experience extremely high visual extinctions, $A_V > 10$ (García-Marín, M. et al. 2009; Piqueras López et al. 2013; Stierwalt et al. 2013), making the optical Hα and Hβ lines poor tracers of star formation (Armus et al. 1989). Extinction across the galaxy is much less severe in the near-infrared (1.6 μm $\sim 0.2 \times A_V$), and lines such as Paα, Paβ, or Brγ can provide a more complete view of the obscured star formation.

In this paper, we present high-resolution (48–112 pc) observations obtained by the Atacama Large Millimeter Array (ALMA) in the 2–1 transition of CO to characterise the properties of GMCs and the local ISM in a sample of nearby LIRGs, which span the entire merger sequence. The star formation associated with the GMCs is estimated from the Hubble Space Telescope (HST) near-infrared (NIR) recombination line images. With these data, we study star formation relations and the effects of the merger environment on the scales of conventionally defined massive GMCs or giant HII regions (e.g. Mivielle-Deschênes et al. 2017).

2. Sample and observations

2.1. Sample selection

We present sub-kpc CO(2–1) observations obtained by ALMA of a representative sample of 27 local LIRGs, which has archival NIR observations from HST. Our sample is drawn from the Great Observatories All-sky LIRG Survey (GOALS; Armus et al. 2009). GOALS is a complete galaxy sample that comprises the 201 LIRG systems ($L_{IR} \geq 10^{11} L_\odot$ and $f_{60\mu m} > 5.24$ Jy) in the IRAS Revised Bright Galaxy Sample (Sanders et al. 2003) and is aimed at measuring the physical properties of local LIRGs across the electromagnetic spectrum using a broad suite of ground- and space-based observatories.

The merger stage classification of our sample is based on Stierwalt et al. (2013), except for three objects (IRAS08355–4944, IRASF13497+0220, IRAS15206–6256), which we have reclassified. The reason for the modification is that the Spitzer classification for these galaxies differs from that based on HST data. While the morphology of some systems in the Spitzer images led to their classification as late-stage mergers, the higher resolution HST data clearly show that the interacting galaxies are in an early merger stage, with minimally disturbed morphologies and no common envelope of stars (the key signature of late-stage mergers). Our sample spans a range of log L_{IR} from 11.16 to 11.73 $L_\odot$, except for one galaxy classified as a ULIRG, with 12.32 $L_\odot$ (see Fig. 1 and Column 8 in Table 1). Five objects are classified as AGN and/or show evidence of AGN activity. In Table 1 we present the main properties of the individual galaxies in the sample.

2.2. CO(2–1) ALMA data

We used ALMA Band 6 observations of the CO(2–1) emission line from ALMA proposal 2017.1.00395.S (PI: T. Díaz-Santos) and completed the sample with the data described in Sánchez-García et al. (2022a). The total sample covers the complete merger sequence of galaxies, where most of the galaxies from Sánchez-García et al. (2022a) are isolated galaxies and early-stage mergers. The data were calibrated using the standard

Table 1: General properties of the sample of Local LIRGs

Object		α	δ	z	D_L	i	log L_{IR}	Spectral	Ref.	Stage
IRAS	Galaxy Name	J2000.0	J2000.0					Class		
		[h m s]	[° ′ ″]		[Mpc]	[°]	[$L_\odot$]			
(1)	(2)	(3)	(4)	(5)	(6)	(7)	(8)	(9)	(10)	(11)
F00163–1039 N	MCG –02–01–052	00 18 49.85	-10 21 34.00	0.0272	117.5	27 ± 1	11.48	H	1,2	2
F00163–1039 S	MCG –02–01–051	00 18 50.90	-10 22 36.7	0.0272	117.5	64 ± 5	11.48	H	1, 2	2
F04315–0840	NGC 1614	04 33 59.95	-08 34 46.6	0.0159	69.7	48 ± 2	11.65	C	3	4
F07160–6215	NGC 2369	07 16 37.73	-62 20 36.4	0.0108	49.7	66 ± 6	11.16	C	3,4	0
08355–4944		08 37 01.87	-49 54 30.0	0.0259	118.0	39 ± 5	11.62	-	5	3
F10015–0614	NGC 3110	10 04 02.11	-06 28 29.5	0.0169	79.5	57 ± 3	11.42	H	3, 5, 6	1
F10257–4339	NGC 3256	10 27 51.30	-43 54 14.0	0.0094	45.7	-	11.64	H	3,4, 5,6	4
F11506–3851	ESO 320-G030	11 53 11.73	-39 07 49.0	0.0108	41.2	56 ± 4	11.17	H	3,4, 5,6	0
F12596–1529 W	MCG -02-33-098 W	13 02 19.66	-15 46 04.2	0.0159	78.7	54± 6	11.17	H	1,5,6	2
F12596–1529 E	MCG -02-33-098 E	13 02 20.38	-15 45 59.6	0.0159	78.7	39 ± 1	11.17	H	1,3, 5,6	2
13120–5453		13 15 06.37	-55 09 22.5	0.0308	144.0	35 ± 6	12.32	Sy2	6	4
F13182+3424	UGC 08387	13 20 35.37	+34 08 22.2	0.0233	110.0	48 ± 4	11.73	L	2	3
F13229–2934	NGC 5135	13 25 44.02	-29 50 00.4	0.0137	60.9	53 ± 9	11.30	Sy2	1, 3,6,7	0
F13370+0105 E	NGC 5258	13 39 57.72	+00 49 53.0	0.0226	108.5	67 ± 3	11.22	H/L	8	2
F13370+0105 W	NGC 5257	13 39 52.95	+00 50 25.9	0.0226	108.5	45 ± 14	11.50	H	8	2
F13497+0220 S	NGC 5331	13 52 16.21	+02 06 05.1	0.0330	155.0	58 ± 2	11.66	-	9	2
F13497+0220 N	NGC 5331	13 52 16.43	+02 06 30.9	0.0330	155.0	66 ± 3	11.66	H	9	2
F14544–4255 W	IC 4518 W	14 57 41.22	-43 07 55.8	0.0159	74.6	50 ± 4	11.24	Sy2	3,7	1
F14544–4255 E	IC 4518 E	14 57 45.33	-43 07 57.0	0.0159	71.2	75 ± 2	11.24	H	6	1
15206–6256 S	ESO 099-G004	15 24 57.98	-63 07 29.4	0.0293	137.0	58 ± 2	11.74			3
15206–6256 N	ESO 099-G004	15 24 58.98	-63 07 29.4	0.0293	137.0	59 ± 1	11.74			3
F16164–0746		16 19 11.75	-07 54 03.0	0.0272	128.0	47 ± 3	11.62	L	6	4
F17138–1017		17 16 35.68	-10 20 40.5	0.0173	76.7	50 ± 1	11.49	H	8	4
F18341–5732	IC 4734	18 38 25.75	-57 29 25.4	0.0157	73.4	58 ± 10	11.35	H	3,6	0
F21453–3511	NGC 7130	21 48 19.54	-34 57 04.7	0.0162	67.6	50 ± 9	11.42	Sy2	6,7	0
F22132–3705	IC 5179	22 16 09.13	-36 50 37.2	0.0114	51.4	62 ± 5	11.24	H	3,6	0
F23007+0836	NGC 7469	23 03 15.64	+08 52 25.5	0.0163	70.8	39 ± 5	11.65	Sy1	3,6	2

Notes. Col. (1): IRAS system name, where an "F" prefix indicates the Faint Source Catalog and no prefix indicates the Point Source Catalog. Col. (2): Galaxy name. Col. (3) and (4): right ascension (hours, minutes, seconds) and declination (degrees, arcminutes, arcseconds) from Stierwalt et al. (2013). Col. (5): Redshift (Stierwalt et al. 2013). Col. (6): Luminosity distance from Armus et al. (2009). Col. (7): Inclination. Col. (8): Infrared luminosity (L_{IR}(8–1000 μm)) calculated from the IRAS flux densities f_{12}, f_{25}, f_{60}, and f_{100} (Stierwalt et al. 2013). Col. (9): Nuclear activity optical spectral class (H = HII region-like, L = LINER, Sy2 = Seyfert 2, Sy1 = Seyfert 1 and C = Composite). Col (10): References of the nuclear classification: 1: Kewley et al. (2001); 2: Veilleux et al. (1995); 3: Alonso-Herrero et al. (2012); 4:Pereira-Santaella et al. (2011); 5: Rodríguez-Zaurín et al. (2011); 6:Pereira-Santaella et al. (2010); 7: Corbett et al. (2003); 8:Yuan et al. (2010); 9: Iono et al. (2005). Col (11): Merger stage based on visual classification: 0 = isolated galaxies, 1 = pairs of galaxies; 2 = early-stage merger, 3 = mid-stage merger, 4 = late-stage merger.

ALMA data reduction software, CASA[1] (McMullin et al. 2007). We subtracted the continuum emission in the *uv* plane using an order 0 baseline. For the cleaning we used the Briggs weighting with a robustness parameter of 0.5 (Briggs 1995), providing a spatial resolution of 48–112 pc. From the 23 LIRGs observed (a total of 27 individual galaxies in the sample when all the galaxies in pairs are counted), 13 were observed using two configurations, compact and extended, and 10 using only the extended configuration. The maximum recoverable scale (MRS) for the compact plus extended configuration data ranges between ∼6″ and ∼11″ (∼1.4 and 3.5 kpc). In the case of the extended-only configuration observations, the MRS is ∼3″ (∼1.1 kpc). In this paper we study spatial scales ∼90 pc, which are 10 times smaller than the MRS, so we expect the missing flux due to the absence of short spacing to be low at these scales. In addition, for a few objects of this sample with single-dish CO(2–1) observations, the integrated ALMA and single-dish fluxes agree within 15% (Pereira-Santaella et al. 2016a,b). The final data cubes have channels of 7.8 MHz (∼10 km s^{-1}) for the sample. The field of view (FoV) of the ALMA single pointing data has a diameter of ∼25″ (∼5-16 kpc). The mosaics have a diameter between ∼38″ and ∼64″ (∼11 and 34 kpc). We applied the primary beam correction to the data cubes. Further details on the observations for each galaxy are listed in Table 2.

A common spatial scale of ∼90 pc was defined in order to have a homogeneous data set. This physical scale was chosen to preserve the original resolution of the nearest objects as much as possible, with minimum degrading, while accommodating only a few most distant sources with a slightly coarser resolution than the common spatial scale. We convolved to 90 pc the data cubes of 30% of the sample with spatial resolutions higher than 80 pc. There are 5 objects (three sources where two of them are galaxy pairs), representing 19% of the sample, with an original resolution of up to ∼110 pc. For these remaining objects, we directly used the cleaned data cubes at their original spatial resolution. We obtained the CO(2–1) moment 0 and 2 maps (see the top and bottom–left panels of Figure 2) using two different methodologies: i) masking pixels in each channel map with fluxes < 3 σ_{CO}, where σ_{CO} is the background noise (for more details, see Sánchez-García et al. (2022a); the code is available on GitHub[2]); and ii) without applying any masking or clipping to the data. We use the first method to follow the methodology of Sánchez-García et al. (2022a) and extend the study to a larger sample of galaxies. With this method, we obtain the brightest emission

[1] http://casa.nrao.edu/

[2] https://github.com/itsmariasg/moment_maps

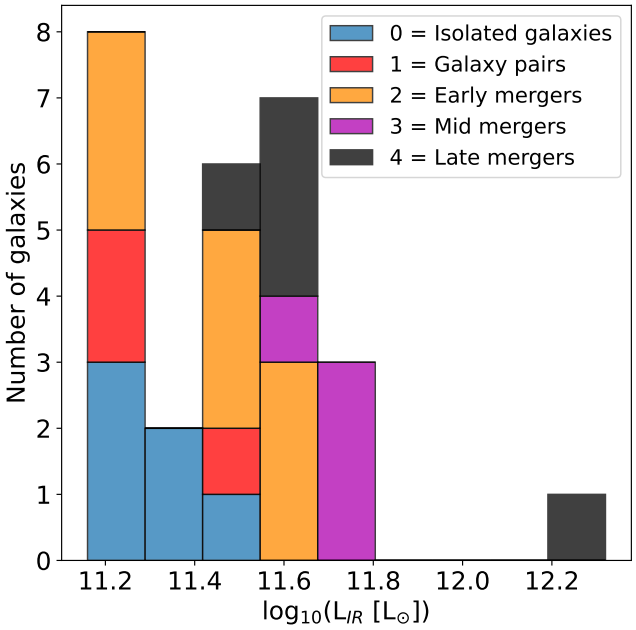

Fig. 1: Stacked histogram showing the distribution of infrared luminosity (L_{IR}) across the different merger stages of the individual galaxies in the sample. The early stages of the merger sequence tend to have lower infrared luminosities, while galaxies in more advanced merger stages predominantly show higher infrared luminosities.

while being restrictive with the noise in the data, whereas we use the second method to include the fainter regions of the clumps.

2.3. HST/NICMOS and HST/WFC3 data

We used the continuum subtracted NIR narrow-band Paα 1.87 μm and Paβ 1.28 μm images taken with the NICMOS and WFC3 instruments, respectively, on board HST to map the distribution of recent star formation in the galaxies of the sample (see Table 2).

These archival HST images are drawn from two projects: Project ID: 10169 (PI: A. Alonso-Herrero) for Paα HST/NICMOS images, and Project ID: 13690 (PI: T. Díaz-Santos) for Paβ HST/WFC3 images. The galaxies from the first project were selected to have a redshift range of 0.0093 $\leq$ z $\leq$ 0.0174, ensuring that the Paα emission line lies within the HST NICMOS F190N narrowband filter (Alonso-Herrero et al. 2006). The FoV of the images is approximately 19″.5×19″.5 (~4.2–7.4 kpc). Galaxies in the Paβ sample (second project) were selected to have redshifts in the range 0.0225 $\leq$ z $\leq$ 0.0352, ensuring that the Paβ emission line lies within the HST WFC3 F132N narrowband filter. The FoV of the latter images is much larger (140″×124″), but most of the Paβ emission is mostly contained within 5 kpc from the galaxy nucleus. For details on the data reduction we refer the reader to Sánchez-García et al. (2022a) for Paα observations and Larson et al. (2020) for Paβ observations.

To obtain the final images, we subtracted the background emission and corrected the astrometry using stars within the NICMOS FoV in the F110W (λ_{eff} = 1.13μm) or F160W (λ_{eff} = 1.60μm) filters and the Gaia DR3 catalogue [3]. Three objects (MCG–02–33–098 E/W, and IC4518 E) do not have Gaia stars in their NICMOS image FoV. In these cases we adjusted the astrometry using likely NICMOS counterparts of the regions detected in the ALMA continuum and CO(2–1) maps. After that, the images were rotated to have the standard north-up, east-left orientation. In order to ensure a consistent comparison between the ALMA and HST data, the Paα and Paβ images (with spatial resolutions of 25–98 pc) were convolved with a Gaussian kernel to match the resolution of the ALMA maps at 90 pc. Only one galaxy has HST data at resolution lower than 90 pc (NGC 5331, where the original spatial resolution was ~98 pc). In this case we convolved the data to the lower angular resolution. The bottom–right panel of Figure 2 shows the final image for NGC3110 (similar figures for the rest of the sample can be found in the database on the Xtreme Scientific Project website [4] [5]).

Most of the galaxies in the Paα sample are isolated galaxies and early-stage mergers; while, mid- to late- stage mergers are covered by the Paβ sample. The combination of the Paα and Paβ samples contains 12 isolated and galaxy pairs, 17 early-stage mergers, and 17 mid- and late-stage mergers. When all the galaxies in pairs are counted, there are a total of 59 individual galaxies in the HST sample. From these, we have ALMA observations at $\lesssim$ 100 pc for 27 individual galaxies (~46% of the sample), with a relatively uniform representation of the entire merger sequence: 6 isolated galaxies, 3 pairs of galaxies and 5 early- (9 individual galaxies), 4 mid- and 5 late-stage mergers.

3. Analysis

3.1. Data analysis

In this section, we describe the two different methodologies used to study the star formation relations in our sample. One focuses on analysing the gas properties along unresolved lines-of-sight, or beam-sized regions, within the galaxies, while the other examines the properties of molecular clouds by identifying and selecting physical clumps and structures. We exclude from our analysis the pixels where AGNs are located by applying a mask.

3.1.1. Beam-sized region analysis

To study the distribution of the cold molecular gas and the recent star formation, we define circular apertures centred on local maxima in the CO(2–1) emission maps, with a diameter of ~90 pc (the spatial resolution of the data). To do so, we first sorted the CO moment 0 pixel intensities. Then we defined circular regions using as centre the pixels in order of descending intensity to prevent any overlap between the regions. With this method we end up with independent, unresolved, non-overlapping regions centred on local emission maxima that cover all the CO emission in each galaxy (see Sánchez-García et al. 2022a). Once we had the regions in CO(2–1) emission maps, we used them on the Paα and Paβ maps to extract the associated star formation rates. We considered Paα and Paβ as detections when the line emission is above 3σ_{Pa}. The σ_{Pa} in these images corresponds to the background noise. In total, we obtain more than 4000 regions for the whole sample. The left panels of Fig. 3 shows an example of the location of the regions on the CO(2–1) (top panel) and Paα (bottom panel) maps of the galaxy NGC 7130 (similar figures for the rest of the sample can be found in the database on the Xtreme Scientific Project website).

[3] http://www.cosmos.esa.int/web/gaia/dr3

[4] https://xtreme.ia.forth.gr/

[5] http://quasar.physics.uoc.gr/xtreme-databases/C-SKDB/figures/

Table 2: ALMA CO(2–1) observations of the sample.

Object	$\theta_{maj} \times \theta_{min}$	θ_m	P.A.	Sensitivity	Mosaics	MRS	FoV	Project	HST image
IRAS Name	[″] [″]	[″, pc]	[°]	[mJy beam^{-1}]		[″]	[″]	PI	
(1)	(2)	(3)	(4)	(5)	(6)	(7)	(8)	(9)	(10)
F00163-1039 N	0.17×0.14	0.15, 83	82	0.53	✓	2.1	64.0	TDS	Paβ
F00163-1039 S	0.15×0.12	0.13, 73	-77	0.53	✓	2.1	38.1	TDS	Paβ
F04315-0840	0.22×0.15	0.19, 61	-74	0.43		11.7	24.8	MPS	Paα
F07160-6215	0.24×0.21	0.23, 48	88	0.51		9.8	24.7	MPS	Paα
08355-4944	0.13×0.10	0.11, 62	57	0.48		1.7	25.1	TDS	Paβ
F10015-0614	0.26×0.21	0.24, 87	-83	0.35		9.6	24.8	MPS	Paα
F10257-4339	0.23×0.21	0.22, 48	63	0.43	✓	5.8	47.4	KS	Paα
F11506-3851	0.30×0.24	0.27, 53	63	0.89		9.1	24.6	LC1	Paα
F12596-1529 W	0.23×0.17	0.20, 74	89	0.48	✓	9.5	48.6	MPS	Paα
F12596-1529 E	0.23×0.17	0.20, 74	89	0.48	✓	9.5	48.6	MPS	Paα
13120-5453	0.15×0.11	0.13, 85	-21	0.57		2.3	25.2	TDS	Paβ
F13182+3424	0.26×0.16	0.21, 106	-16	0.43		3.3	25.0	TDS	Paβ
F13229-2934	0.31×0.22	0.27, 76	63	0.21		10.2	24.8	LC2	Paα
F13373+0105 E	0.19×0.14	0.17, 84	-83	0.59	✓	2.6	50.6	TDS	Paβ
F13373+0105 W	0.19×0.14	0.17, 84	-83	0.60	✓	2.6	50.6	TDS	Paβ
F13497+0220 S	0.17×0.14	0.16, 112	-82	0.33	✓	2.6	46.1	TDS	Paβ
F13497+0220 N	0.17×0.14	0.16, 112	-82	0.38	✓	2.6	38.5	TDS	Paβ
F14544-4255 W	0.23×0.20	0.22, 76	-86	0.46		10.7	24.8	MPS	Paα
F14544-4255 E	0.23×0.20	0.22, 73	-87	0.47		10.7	24.8	MPS	Paα
15206-6256 S	0.18×0.16	0.17, 106	-5	0.37	✓	3.0	38.4	TDS	Paβ
15206-6256 N	0.18×0.16	0.17, 106	-5	0.37	✓	3.0	38.4	TDS	Paβ
F16164-0746	0.14×0.11	0.13, 76	-57	0.43		2.1	25.1	TDS	Paβ
F17138-1017	0.26×0.22	0.24, 87	-62	0.75		7.8	24.8	MPS	Paα
F18341-5732	0.19×0.16	0.18, 62	-60	0.77		2.7	24.8	TDS	Paα
F21453-3511	0.26×0.22	0.24, 87	-62	0.29		10.5	24.8	MPS	Paα
F22132-3705	0.17×0.16	0.17, 42	-61	0.45		9.8	24.7	MPS	Paα
F23007+0836	0.16×0.12	0.14, 46	-48	0.29	✓	2.9	38.0	TDS	Paα

Notes. Col. (1): IRAS denomination from Sanders et al. (2003). Col. (2): major (θ_{maj}) and minor (θ_{min}) FWHM beam sizes. Col. (3): mean FWHM beam size (θ_m) in arcseconds and parsecs, respectively. Col. (4): position angle (P.A.) in degrees. Col. (5): 1σ line sensitivity per channel (width of $\sim$ 10 km/s) of the CO(2–1) observations. Col. (6): ✓galaxies with mosaics. Col. (7): Maximum recoverable scales. Col. (8): Field of view. Col. (9): Principal investigator of the ALMA project: MPS: Miguel Pereira-Santaella (2017.1.00255.S), KS: Kazimierz Sliwa (2015.1.00714.S), LC1: Luis Colina (2013.1.00271.S), LC2: Luis Colina (2013.1.00243.S) and TDS: Tanio Díaz-Santos (2017.1.00395.S) Col (10): H recombination line HST images.

3.1.2. Dendrogram analysis

Our data allow us to study molecular gas at scales of ∼90 pc, enabling the characterisation of the properties that define molecular clouds in LIRGs. The sizes of molecular clouds in galaxies are on the order of 50 to 150 pc (e.g. Miville-Deschênes et al. 2017; Oey et al. 2003; Bolatto et al. 2008). To identify physical clumps and measure their properties, we use the Python code `Astrodendro` (Rosolowsky et al. 2008). This algorithm enables the study of the hierarchical structure of the CO(2–1) emission from molecular clouds. We also apply this structure to the HST recombination line images to extract the associated star formation rates. The dendrogram algorithms build a tree structure that is separated into three categories: leaves, branches, and trunks. The process begins with the brightest pixels in the dataset, progressively adding fainter pixels and creating small structures (referred to as leaves). If the intensities of two or more non-contiguous structures differ by more than a given threshold, they are considered separate entities. Low-density gas is represented at the bottom of the hierarchical structure in a dendrogram, the initial branch of the structure (referred to as trunk). This initial branch (trunk) connects to other branches and leaves. Thus, leaves are the most isolated category, with no substructure. We associate the leaves with molecular clouds/clumps in the case of the ALMA CO(2–1) maps.

The identification of clouds/clumps depends on three inputs: (i) the minimum flux value per pixel to consider in the dataset; no value lower than this will be considered in the dendrogram (`min_value`); (ii) how significant a leaf has to be with respect to other already detected leaves or branches in order to be considered an independent structure (`min_delta`). The significance is measured from the difference between its peak flux and the value at which it is being merged into the tree, and (iii) the minimum number of pixels (equivalent to an area) needed for a leaf to be considered an independent entity (`min_npix`). We use the following conditions to identify clouds/clumps in our galaxy sample: `min_value` = 1σ (see below for further constraints), `min_delta` = 1σ, `min_npix` = 80% of a beam (PSF) area for ALMA data.

After creating the clump catalog based on the CO(2–1) emission maps, we measure the hydrogen recombination line emission from the Paα and Paβ maps using the same spatial coordinates and leaf structures identified in the CO(2–1) clumps. In this case we considered Paα and Paβ detections when the associated structures are above $3\sigma_{Pa}$. To avoid noise spikes, we lastly consider the criterion that the CO clumps have an emission greater

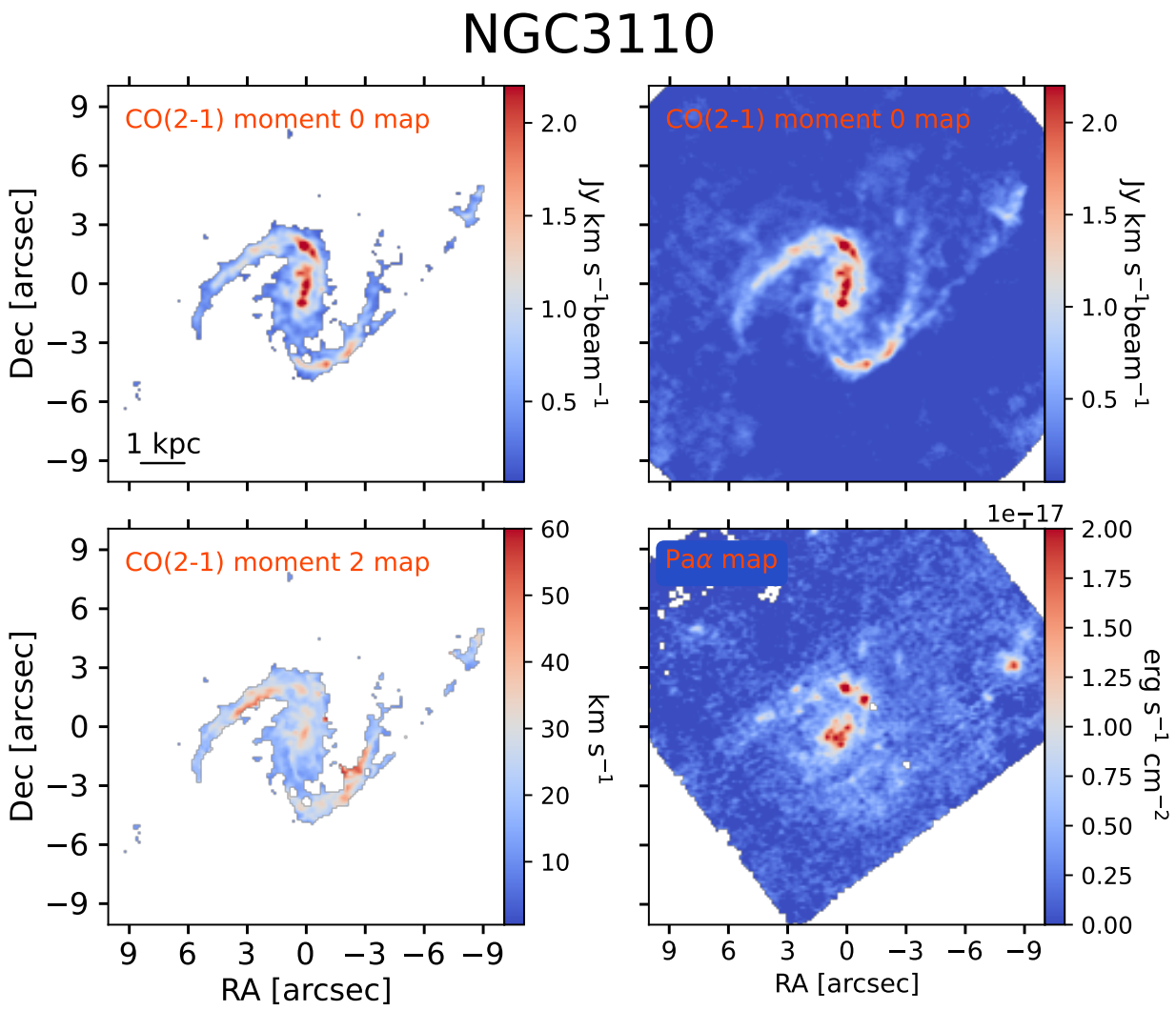

Fig. 2: ALMA CO(2–1) integrated intensity (moment 0) maps, with pixel masking applied to the data cube (top left panel) and without it (top right panel), CO(2–1) velocity dispersion (moment 2) map (bottom left panel) and the HST Paα image (bottom right panel) of the galaxy NGC 3110 at 90 pc scale. At this scale, significant differences are observed between the CO(2–1) moment 0 and Paα maps, revealing emission structures distributed throughout the galaxy.

than $3\sigma_{CO}$, since we used a `min_value` input of $1\sigma_{CO}$ to allow the detection of emission from potentially more diffuse clumps. Considering this, we identify a total of 1027 clumps in our sample of galaxies.

The validation of this method using observations from one and two array configurations is presented in Appendix A. We compared images obtained with a long baseline array and with a combination of long and short baseline arrays. We find no significant difference in the clump identification.

The right panels of Fig. 3 shows an example of the location of the clumps on the CO(2–1) (top panel) and Paα (bottom panel) maps of the galaxy NGC 7130. Fig. 4 shows the distribution of the number of gas clumps per galaxy across the different merger stages. This figure suggests that galaxies at early stages of the merger sequence (isolated galaxies, galaxy pairs and early mergers) contain from just a few dozen clumps to over 100 clumps within them, while galaxies in more advanced merger stages host comparatively lower (N<40) number of clumps per galaxy.

3.2. Calculating physical properties

We measure the physical properties of each region and clump where CO and Paα/Paβ are detected, following the analysis of Sect. 3.1.1 and 3.1.2. For both methods we calculate the mass, velocity dispersion of the gas, star formation rate and molecular gas surface densities, the boundedness of the gas, star formation efficiency and the gas depletion time scale. Furthermore, we estimate the effective radius for each clump. All these parameters are detailed below. We refer to quantities computed via beam-sized region analysis as $X_{regions}$ and via dendrogram analysis as X_{clumps}.

To estimate the cold molecular gas mass in the beam-sized regions and clumps, we use a CO(2–1)/CO(1–0) ratio (R_{21}) of 0.7, obtained from single-dish CO data of the LIRG IC 4687 (Albrecht et al. 2007). This R_{21} value is within the range found by Garay et al. (1993) and Montoya Arroyave et al. (2023) for infrared galaxies. We also use a Galactic CO-to-H_2 conversion factor, $\alpha_{CO}^{1-0} = 4.35\ M_\odot pc^{-2}(K\ km\ s^{-1})^{-1}$ (Bolatto et al. 2013). A detailed analysis about the effects of using different α_{CO} values on the results of this work is provided in Appendix B. How-

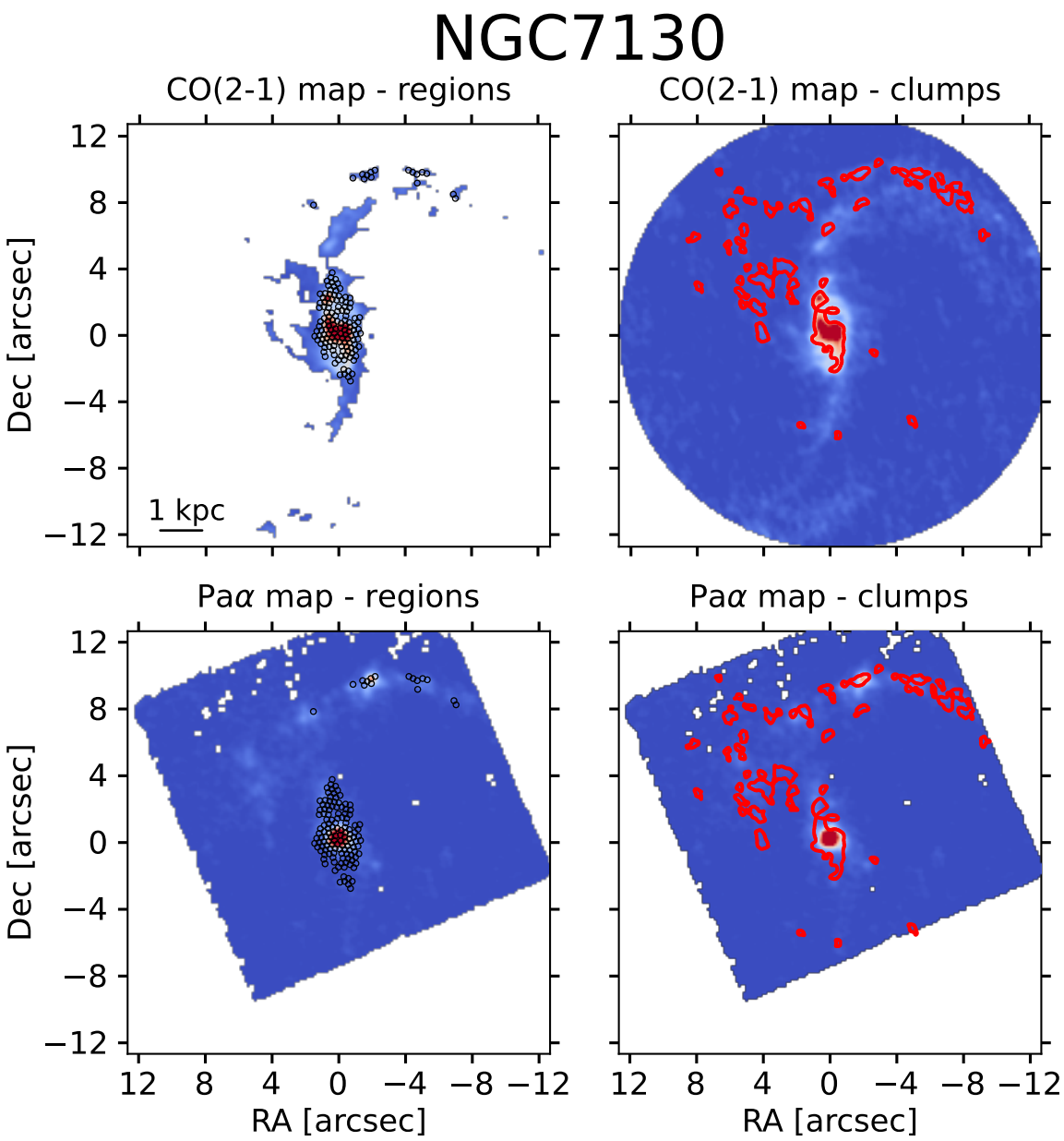

Fig. 3: ALMA CO(2–1) integrated intensity (moment 0) map and HST Paα image of the galaxy NGC7130. Left: Location of the beam-sized regions (in black) on the CO(2–1) (top) and Paα (bottom) maps. Right: Location of physical structures (in red) found using Astrodendro (clumps) on the CO(2–1) (top) map, also projected over the Paα (bottom) map. The regions and clumps are both detected with ALMA and HST, considering the conditions described in Section 3.1.

ever, as argued below, we do not expect that a lower conversion, factor typical of ULIRGs (Papadopoulos et al. 2012), is appropriate for our targets. The galaxies in our sample have a mean infrared luminosity of $\log(L_{IR}/L_{\odot})$=11.48. In addition, most of the galaxies in our sample show a mean effective radius of the large scale molecular component (R_{CO}^{eff}) of 740 pc (Bellocchi et al. 2022), while local ULIRGs show a mean value of R_{CO}^{eff} = 340 pc (Pereira-Santaella et al. 2021). Therefore, it is likely that the α_{CO} of our sample is similar to that of normal galaxies, rather than the lower value typically observed in local ULIRGs (but see Saito et al. 2017; Herrero-Illana et al. 2019). The CO-to-H_2 conversion factor can also be affected by the metallicity of the galaxies, showing higher values with decreasing metallicity (α_{CO} = 4.35 $(Z/Z_{\odot})^{-1.6}$ $M_{\odot}pc^{-2}(K\ km\ s^{-1})^{-1}$, Accurso et al. 2017). Rich et al. (2012) studied the metallicity in some local (U)LIRGs, showing a decrease in the abundance with increasing radius. In the case of the metallicity in local disks, Sánchez et al. (2014) observed a similar behaviour. Based on these works, the expected variation in the conversion factor due to metallicity gradients at $r < 5$ kpc is 20-30%. Finally, we calculate the molecular gas mass surface density (Σ_{H_2}).

To determine the SFR and SFR surface density (Σ_{SFR}) of the beam-sized regions and clumps detected in our galaxies, we use the Hα calibration (Kennicutt & Evans 2012), which assumes a Kroupa (2001) initial mass function, and a Hα/Paα ratio of 8.6 and a Hα/Paβ ratio of 17.6 (case B at T_e = 10.000 K and $n_e = 10^4$ cm^{-3}, Osterbrock & Ferland 2006). To correct the Paα and Paβ emission for dust attenuation for each region and clump, we use

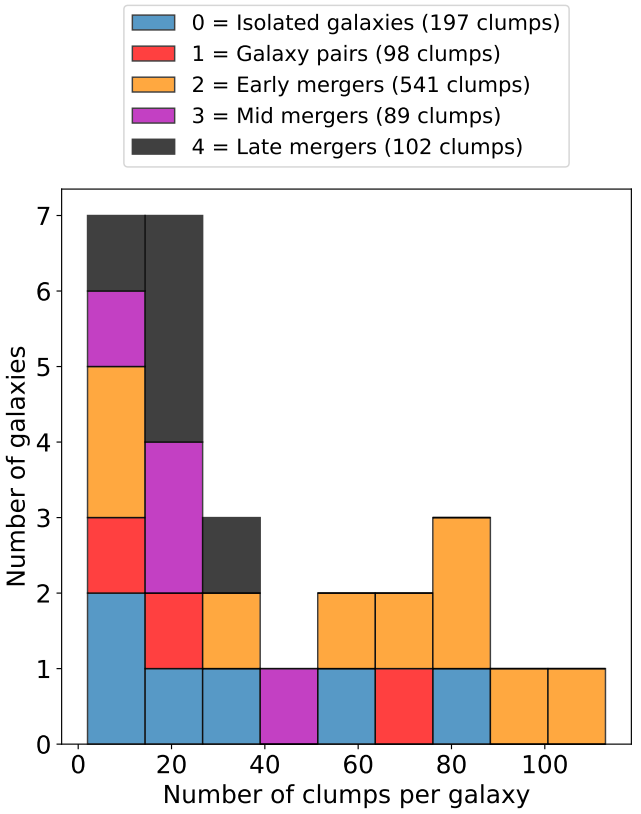

Fig. 4: Distribution of the number of CO clumps per galaxy across the different merger stages in the galaxy sample. The early stages of the merger sequence cover the entire range of the stacked histogram, while galaxies in more advanced merger stages contain a lower number of clumps per galaxy.

the Brδ and Brγ line maps observed with the SINFONI instrument on the Very Large Telescope (VLT) to derive A_K. These maps have effective FoV between $8'' \times 8''$ and $12'' \times 12''$ (Piqueras López et al. 2013). The estimated A_K values in this work range from 0.95 ± 0.60 to 1.98 ± 1.29 mag. For an in-depth explanation of the extinction correction method, we refer the reader to Sánchez-García et al. (2022a).

All the Σ_{H_2} and Σ_{SFR} values are corrected for the inclination of each galaxy (see Table 1, Column (7)). The inclination is estimated from Spitzer 3.6 μm band images, which have a PSF of $\sim 1.7''$, as presented in Pereira-Santaella et al. (2011). We define the inclination (i) of a galaxy as

$$i = \cos^{-1}(b_{sm}/a_{sm}) \quad (1)$$

where b_{sm} and a_{sm} are the lengths of the minor and major semi-axes of the object, respectively. We use the elliptical isophote fitting from the `isophote`[6] package in Python, which provides the values of the major and minor semi-axis lengths for each fitted ellipse. Finally, the inclination value is determined as the mean inclination of the fitted ellipses that are unaffected by the PSF of the images or the structure of the galaxy. The uncertainty in the inclination is calculated as the standard deviation of the inclinations of the considered ellipses.

Both the SFR and the cold molecular gas surface density estimates are affected by flux calibration errors. We assume an uncertainty of about 10% for the ALMA fluxes (see ALMA Technical Handbook [7]), and ∼15–20% for the NICMOS fluxes (Alonso-Herrero et al. 2006; Böker et al. 1999).

We also explore other properties of the molecular gas: the velocity dispersion (σ_{gas}) obtained from the CO(2–1) moment 2, and the dynamical state of molecular gas in the beam-sized regions and clumps using the boundedness parameter

$$b \equiv \Sigma_{mol}/\sigma^2 \propto \alpha_{vir}^{-1}, \quad (2)$$

where σ is the velocity dispersion and α_{vir} the virial parameter. That is, low values of b indicate that gas clumps is supported against gravity by their internal velocity dispersion, while large values of b are representative of clumps that are unstable against gravitational collapse. Finally, we calculate the gas depletion time as $t_{\rm dep} = \Sigma_{H_2}/\Sigma_{SFR}$ and the star formation efficiency as SFE = $t_{\rm dep}^{-1}$. The effective radius of the gas clumps is calculated from the area of the clumps, as determined by the Astrodendro algorithm.

4. Results and discussion

In total, we define more than 4000 beam-sized regions across the whole sample (27 objects), and consider more than 1000 molecular gas clumps using Astrodendro. The sizes of these molecular gas clumps range from 89 to 694 pc, except for a clump in the galaxy IRAS15206-6256-N, which reaches 1068 pc. The median clump size in our sample is 154 pc. The number of clumps and regions per LIRG varies across the sample galaxies (see Figs. 4 and C.2).

These cloud-scale observations reflect both the typical locations where stars form and regions with more extreme conditions than those found in star-forming galaxies. A detailed analysis about the lifecycle of clouds will be studied in Sánchez-García et al. (in prep.). In this work, we focus on scaling relations between ISM and resolved clump properties.

4.1. Resolved star-formation properties in LIRGs

4.1.1. Kennicutt-Schmidt law

We study the molecular KS relation for each galaxy at a resolution of 90 pc using beam-sized regions and clumps. As an example, Fig. 5 shows the Σ_{SFR} as a function of Σ_{H2} for NGC 3110 and NGC 7469 (similar figures for the rest of the sample can be found in the database on the Xtreme Scientific Project website). The KS diagram using beam-sized regions in NGC 3110 (top left panel) suggests that these regions follow two different power laws. These two branches were identified using the Multivariate Adaptive Regression Splines (MARS, Friedman 1991) fit, which gives the position of the breaking points for a linear regression with multiple slopes. The branch with higher gas and SFR densities is located in the central region of the galaxy, and shows a superlinear slope, while the other branch with lower gas and SFR densities is located in the more external disk regions, with a sublinear slope. The spatial distribution in the dual galaxy NGC 3110 is shown in Figure C.1, Appendix C.1. This behaviour is observed in 9 galaxies (∼33%) of our galaxy sample. These dual galaxies span the merger sequence as follows: 22% are isolated galaxies, 12% are galaxy pairs, and each of early-, mid-, and late-stage mergers accounts for 22%. Regarding their nuclear activity classification, 45% of the dual galaxies exhibit HII region-like activity, 22% are classified as Seyfert 2,

[6] https://photutils.readthedocs.io/en/latest/user_guide/isophote.html

[7] http://almascience.eso.org/documents-and-tools/latest/documents-and-tools/cycle8/alma-technical-handbook

while LINERs and composite account for 11% each. The duality is reinforced if we consider a factor α_{CO} = 0.8 (Downes & Solomon 1998) typical of ULIRGs in the central regions of our sample. For the case of the clump selection (top right panel), the data points follow a single power-law.

Similarly, the KS diagram for NGC 7469, using the beam-sized region selection (bottom left panel), also suggests that the data points follow a single power-law. A comparable result is observed with the clump selection (bottom right panel). Thus, LIRGs exhibit two distinct behaviours when analysed using the beam-sized selection method, consistent with Sánchez-García et al. (2022a), which they refer to as dual and non-dual behaviour. However, only a single behaviour is evident when the clumps are identified using Astrodendro. We fit the data points using the orthogonal distance regression (ODR, Boggs et al. 1987) method, which minimizes the orthogonal distances from the data points to the regression line.

The absence of a dual slope (the steeper slope) in the KS relation may be related to the scarcity of clumps identified by astrodendro in the central kpc of galaxies with dual behaviour. One possible explanation for this can be that there is a limitation in the identification of structures in the central regions of dual galaxies. These galaxies can host very dense cores, with numerous clumps distributed along the line of sight which cannot be resolved at the angular resolution of the current data. An example of this is shown in right panel of Figure 3, where we see a large, resolved single clump at the centre of the galaxy. This interpretation is consistent with the scenario suggested by Díaz-Santos et al. (2017), who observed an increased compaction of gas and dust in some LIRGs that could correspond to the extreme dynamical environment found in the central kpc of dual galaxies. Higher resolution observations are needed in order to disentangle physical gas clumps at the core of these galaxies.

As expected, these two methods show variations in both the slope and the correlation coefficient, with steeper slopes and stronger correlations observed when studying physical structures in galaxies with a non-dual behaviour. Around 70% of the objects show a steeper slope and more than 50% show a better correlation with the clump selection method. This result may be due to the fact that we are now studying physical structures where star formation is produced, in contrast to the region-based method, where we examine the molecular gas present in each galaxy. In the latter method, this does not imply that star formation occurs in all gas regions across the galaxy.

We do not include in our analysis upper limits. Pessa et al. (2021) studied the influence of non-detections in several resolved scaling relations. In principle, non-detections could artificially flatten the relations at small spatial scales, resulting in a steepening when the analysis is carried out at larger spatial scales, as pixels with signal would be averaged with the non-detection pixels at larger scales. In turn, they found that ignoring the non-detections have a small impact on the measured slope.

Zetterlund et al. (2019) studied how the properties of a set of Galactic GMCs correlate with the local SFR using Astrodendro. They found a steep slope of N=2 in the KS diagram. In our sample we obtain a wide range of slopes from sub-linear (0.39±0.07) up to super-linear (3.36±0.44). However, Demachi et al. (2024) studied the GMCs properties using the PHANGS galaxy M74 with a resolution of 50 pc, finding a large dispersion in the relation. Their results suggested that the law breaks down at a GMC scale of < 100 pc. This contrasts with the results obtained in this work, where we observe a strong correlation (ρ_s>0.7) for most of the galaxies in the sample. This discrepancy could arise from the fact that in M74, the identified structures are on average smaller and may represent substructures of the GMCs, producing the large dispersion due to the different evolutionary stage of these substructures. In other words, this galaxy may not exhibit the same limitations in the identification of structures as those observed in the central regions of our sample. Another possible explanation for the scatter is that star-forming galaxies like M74 may host numerous clumps where the star formation process is less efficient compared to LIRGs. Kreckel et al. (2018) measured that only 22% of the GMCs host associated SF, with 40% of those having two or more associated HII regions in NGC 628. This could result in a wider range of dispersion on the y-axis of the KS diagram.

4.1.2. Self gravity of the gas

We explore the dynamical state of the molecular gas using the boundedness parameter of gas in regions ($b_{regions}$) and clumps (b_{clumps}). Figure 6 shows the spatial distribution of the boundedness parameter (b) and SFE ($t_{\rm dep}^{-1}$)(panels left and middle, respectively) based on the clumps and beam-sized regions identification (top and bottom row, respectively) for the galaxy IRASF17138–1017. We observe higher self-gravity of the gas in specific parts of the galaxy, most of which are located in the central and eastern parts. Furthermore, clumps in these locations exhibit higher self-gravity and star formation efficiency. We observe an agreement between the $b_{regions}$ and the b_{clumps}.

Different trends are observed when representing the cold molecular gas depletion time as a function of the gas boundedness parameter, using the two methods in individual galaxies. These trends range from clearly negative correlations (e.g., NGC 7469 and NGC 1614) to positive correlations (e.g., IRASF 13373+0105A/B), see the figures in the Xtreme Scientific Project database. However, for most galaxies, a general trend of decreasing $t_{\rm dep}$ with increasing b is observed. Leroy et al. (2017) studied the cloud-scale ISM at a resolution of 40 pc distributed over ~ 370 pc scales in the galaxy M51. They found that gas with larger b (more bounded) exhibits shorter $t_{\rm dep}$, suggesting that increased self-gravity promotes higher star formation efficiency. However, Kreckel et al. (2018) did not find any correlation between b and $t_{\rm dep}$ in another spiral (NGC 628) at a resolution of 50 pc over scales of 500 pc. In our work, we find different trends, indicating that, as reported in previous works, the behaviour of self-gravity of the gas with depletion time varies for each galaxy. The depletion times in our sample are 4, and up to 8 times shorter than in these two spirals. For a lower α_{CO} value, we would obtain an even shorter $t_{\rm dep}$. We obtain median depletion timescales of 0.2−1.2 Gyr in our sample using a Galactic α_{CO} conversion factor. For the galaxy M51, depletion times vary between 1.5 and 2 Gyr, while for NGC 628, the median depletion time ranges between 1 and 3 Gyr. This difference is consistent with what was found in previous works for starbursts (Daddi et al. 2010; Genzel et al. 2010; García-Burillo et al. 2012; Sánchez-García et al. 2022a).

4.1.3. Velocity dispersion of the gas

In this section, we explore the behaviour of the velocity dispersion of the gas in our sample. The right panels of Fig. 6 show the spatial distribution of the velocity dispersion of the gas (σ_{gas}) for the galaxy IRASF17138–1017 based on the clump and beam sized regions identification (top and bottom panels, respectively). We find an anticorrelation between the SFE and the velocity dispersion of the gas. Therefore when the velocity dis-

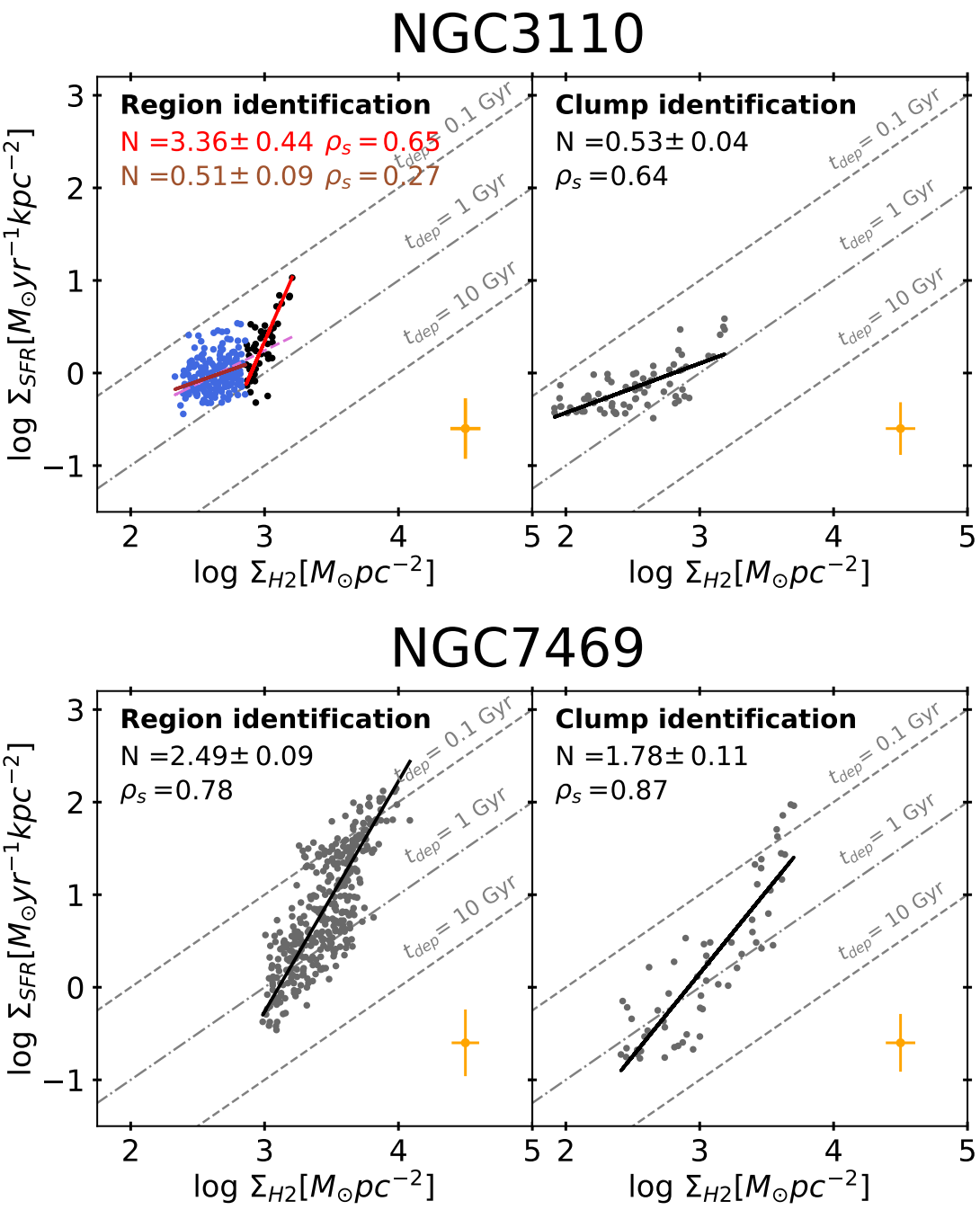

Fig. 5: The SFR surface density (Σ_{SFR}) as a function of the molecular gas surface density (Σ_{H2}) is shown using beam-sized regions (left) and clumps identified with Astrodendro (right) for NGC 3110 (top) and NGC 7469 (bottom). The blue and black points represent the two branches derived by applying the MARS method with breaking points in the log Σ_{H2} for NGC3110 in the case of regions. The dark gray points correspond to the clumps method. The brown and red solid lines are the best fit for the two branches, while the black line represents a one-slope fit. The Spearman's rank correlation coefficients (ρ_s) and the power-law indices (N) of the derived best-fit KS relations in the top-left of each panel. The error bars indicate the mean systematic uncertainties in Σ_{H2} of ± 0.11 (0.10) dex (horizontal) and the extinction correction in Σ_{SFR} of ± 0.27 (0.29) dex (vertical) for NGC 3110 (NGC 7469). The grey dashed lines mark constant gas depletion times ($t_{\rm dep} = \Sigma_{H2}/\Sigma_{SFR}$).

persion of the clumps is higher, these clumps are less efficient to form stars. We observe variations in σ_{gas} and SFE within the galaxies. The velocity dispersion of the clumps is higher in the northern part of the central disk of the galaxy, while the southern part of the central disk is more efficient. These variations indicate different dynamical environments throughout the galaxy. We observe a general agreement between the two methods.

On the other hand, we find positive correlation between the SFE and the velocity dispersion of the gas in other galaxies such as NGC 7130 and NCG 2369, where the clumps with higher velocity dispersion are more efficient. In the second galaxy we see

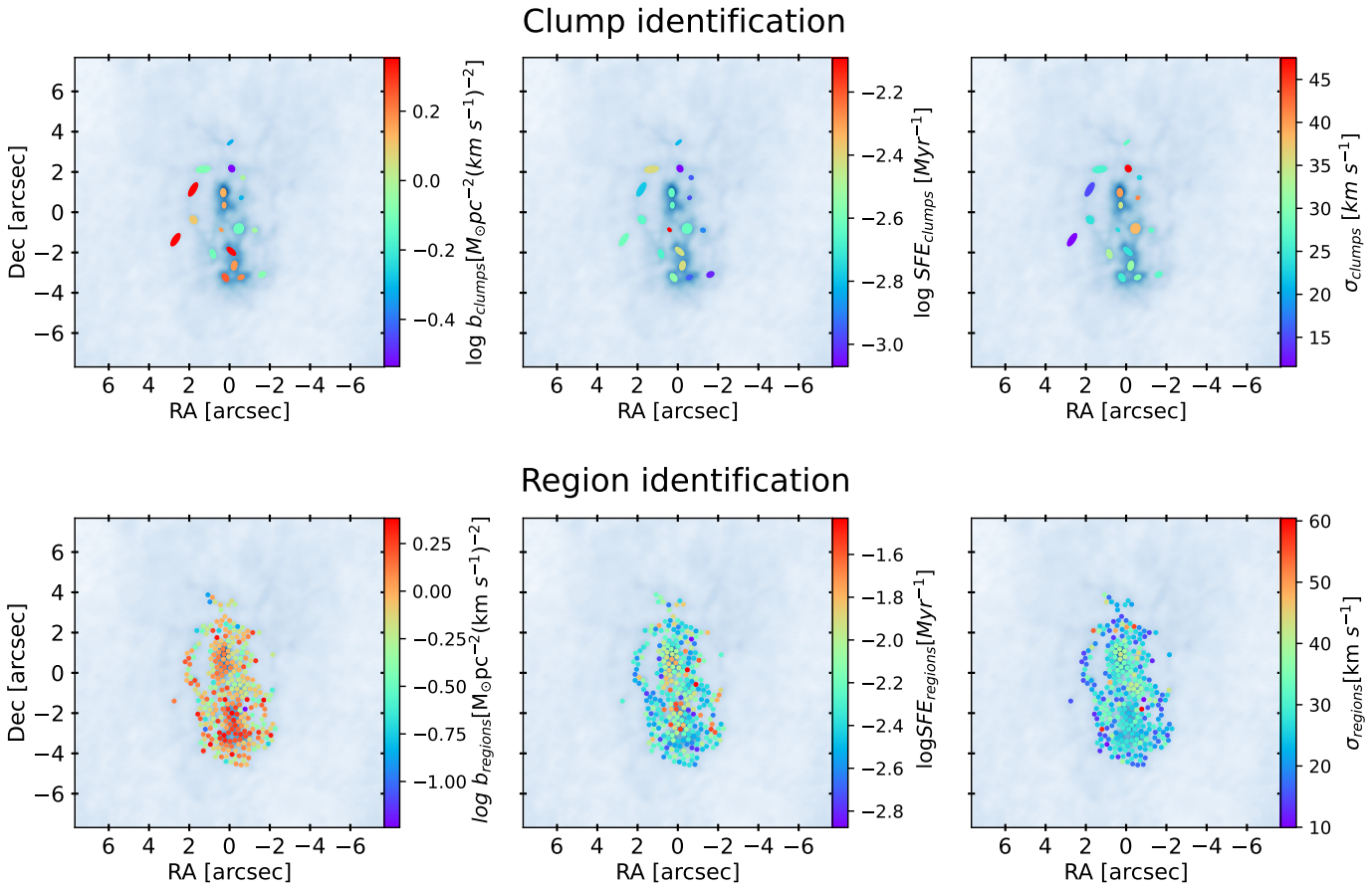

Fig. 6: Maps of the boundedness parameter, b_{clumps} (top left) and $b_{regions}$ (bottom left), as well as maps of the star formation efficiency, SFE_{clumps} (top middle) and $SFE_{regions}$ (bottom middle), and the velocity dispersion, σ_{clumps} (top right), and $\sigma_{regions}$ (bottom right) of the gas for the galaxy IRASF17138–1017. Both methods yield comparable results, as evidenced by the spatial distribution of the regions and clumps within the galaxy.

higher velocity dispersion in the centre where the gas is more efficient (see the figures in the Xtreme Scientific Project database). However, a universal trend is not found. The differences lie in some galaxies exhibiting higher velocity dispersion values at their centres, while others show higher values in their outer regions. This may be attributed to the influence of the surrounding environment of each galaxy (e.g., interactions and mergers with other galaxies) as well as to their internal structure (e.g., spiral arms, corotation, etc.), which contribute to the range of trends seen in our sample.

4.2. Star formation properties as a function of merger stage

We aim to investigate the potential influence of the merger process on the star formation in galaxies. While morphological differences are well-known, this study seeks to understand whether and how the merger stage impacts star formation and the environment of molecular clouds, thereby enhancing and/or suppressing the efficiency of new star formation. In this section, we focus on the study of clumps, while the figures of results obtained with the regions will be referred to the reader in the Appendix C.2.

4.2.1. Kennicutt-Schimdt law across the merger sequence

We investigate the star formation relation as a function of the merger stage of the galaxies in our sample. When analysing the KS diagram using clump identification (Fig. 7), we find that the slope of the correlation is mostly linear or sublinear in the early interacting stages of the merger sequence (isolated galaxies and galaxy pairs). However, as the merger progresses to more advanced stages, the slope becomes superlinear (steeper), implying a change in behaviour in the efficiency of converting molecular gas to stars. Moreover, as shown in Figure 7, the correlations vary with the merger stage. Table 3 presents the correlation coefficient, mean values, and KS relation slope for merger stages in both beam-sized regions and clumps.

When exploring the KS relation using beam-sized regions (see Figure C.3 in Appendix C.2), we find that the slope values remain close to one in all cases and do not vary significantly throughout the merger sequence. This suggests that, when considering the gas and star-forming emission of galaxies without identifying physical structures such as clumps or clouds, the relationship between the surface densities of gas and SFR does not evolve with the merger stage. It is only when physical structures (clumps) are selected that we observe an evolution in the KS slope, with mid- and late-stage mergers exhibiting clumps with nearly an order of magnitude shorter depletion time scales than those in earlier interaction stages. In contrast, the uniform slope observed using the beam-sized regions method likely re-

flects the influence of the larger gas disk across the full extent of the galaxy, as these unresolved lines-of-sight include emission regions across the entire gas structure of the galaxies that are much more diffuse than those probed by the physical clumps. These results are consistent with high-resolution hydrodynamic simulations that investigate how galaxy mergers affect the structure of the ISM and the properties of GMCs and young massive clusters (Li et al. 2022), as well as simulations that study the properties of young star clusters formed under different ISM conditions within a galaxy (Grudić et al. 2022).

The mean values of $\log_{10}\Sigma_{H2}$ and $\log_{10}\Sigma_{SFR}$ for each merger stage, calculated using the two different methods described in this work, show differences (see Fig. 8). For isolated galaxies, galaxy pairs, and early-stage mergers, the mean values obtained through the region selection method are slightly higher than those derived from the clump-based method (see Table 3). For late-stage mergers, however, both methods (clump and region selection) yield similar results. When comparing the mean values across merger stages using the clump selection method, we observe a gap of more than 0.5 dex between late-stage mergers and earlier stages. These results indicate variations throughout the merger sequence, with higher values of Σ_{SFR} and Σ_{H2} in late-stage mergers compared to earlier interaction stages. These differences may result from the merger sequence in galaxies, where isolated galaxies and early interactions exhibit lower amounts of gas and star formation. As the merger progresses, however, the amount of gas in the central kiloparsecs of the galaxy undergoing the merger increases, along with the SFR.

4.2.2. Self gravity across the merger sequence

Figure 9 shows the cold molecular gas depletion time, $t_{\rm dep}$, as a function of the self-gravity of the clumps given by the b parameter. We observe a shift in the trend from positive to negative correlations as the merger progresses, with the strength of the anti-correlation increasing at the later stages of interaction. This indicates that, in later merger stages, the self-gravity of the clumps generally have high values (most show $b_{clumps} \gtrsim 1$), and those that are more bound are also more efficient at forming stars, exhibiting shorter gas depletion timescales. The study of the self-gravity of the gas in individual galaxies reveals a variety of results (see Sect. 4.1.2). However, the picture changes when considering the merger stage of galaxies, and some trends emerge. The average $t_{\rm dep}$ across the merger stages does not change significantly, but the boundedness and its relation with $t_{\rm dep}$ evolve strongly (see Table 4 and the bottom-right panel of Figure 9).

There are some differences between the results obtained with clump and region selections (see Figure 4 for clumps and Figure C.4 for regions). This discrepancy may arise from the fact that the region-based approach examines gas emission and star formation rates across the entire galaxy, while the clump-based method focuses on the properties of physical structures where star formation occurs.

The region selection provides more information about the dynamic environment of molecular clouds, offering insights into, for example, the inter-cloud turbulence (see Sect. 4.2.3). In contrast, the clump approach allows us to study the characteristics of physical structures where stars are currently forming, have already formed, or will form in the future.

4.2.3. Velocity dispersion of the gas across the merger sequence

Several SF models suggest that the dynamical state of the cloud, and not only its density, affects its ability to collapse and form stars (e.g. Krumholz & McKee 2005; Hennebelle & Chabrier 2011; Federrath & Klessen 2013). These models focus on the properties of turbulent molecular clouds, proposing that the supersonic and compressive turbulence induces the formation of stars. In this case we would expect the SFE to increase with increasing gas velocity dispersion (Orkisz et al. 2017).

Figure 10 shows the SFE as a function of the velocity dispersion of the clumps (σ_{clumps}) across the merger sequence. We observe that clumps in galaxy pairs, early-stage mergers, and specially mid-stage mergers exhibit higher velocity dispersion than those in isolated galaxies and late-stage mergers. However, early-stage mergers exhibit significant scatter along both axes of the diagram. Additionally, we observe that clumps with high velocity dispersion are not necessarily more efficient at forming stars. In mid-stage mergers, the SFE decreases with increasing velocity dispersion of the clumps, contrary to the theoretical predictions mentioned above. In contrast, this anticorrelation is not observed in other merger stages (see Figure 10). This result could be attributed to the presence of shocks resulting from the active merger, where elevated turbulence, likely driven by galaxy-wide shocks, reduces the efficiency of star formation during this chaotic stage (see Saito et al. 2017), as the gas has not yet settled down. In late-stage mergers, clumps exhibit the lowest velocity dispersion among all merger stages, with a very narrow range of values. Still, the range of SFE is similar to that of mid-stage mergers.

4.2.4. Interpretation

A possible explanation for the different trends observed across the merger sequence between the SFE (t_{dep}^{-1}) and b parameter, and velocity dispersion is that in isolated galaxies or galaxy pairs, the influence of the interaction is still minimal or negligible. In these cases, clumps show high values of boundedness of the gas and/or high velocity dispersion, but they do not exhibit trends between t_{dep} and self-gravity of the gas (Fig. 9) or between SFE and velocity dispersion (Fig. 10). However, as the interaction between galaxies becomes more pronounced—producing tidal tails, highly distorted morphologies, and a more chaotic environments—the velocity dispersion of the gas increases, likely driven by turbulence in the clumps. This, along with the large gas content, enhances the self-gravity of the gas, making the clumps more efficient at forming stars. Comparatively, late-stage mergers do not exhibit high velocity dispersion values (Fig. 10), yet they still contain large amounts of molecular gas (Fig. 8). These clumps can still result in high star formation efficiencies.

This interpretation also agrees with SMUGGLE simulations (Li et al. 2022). These simulations show that cluster mass increases with increasing tidal field strength. The increase in mass-weighted gas pressure leads to a higher fraction of bound GMCs, which is necessary for star formation under these conditions, resulting in high SFE. Interestingly, clumps with high boundedness, and large amounts of molecular gas and higher pressure are located in the central regions of the mergers, which is precisely where we observe steeper KS slopes and higher SFE. We know, however, that stellar bars and/or spiral arms, as well as AGN activity—some of which may be heavily buried, particularly in late stages (e.g. Ricci et al. 2021)—can influence the star

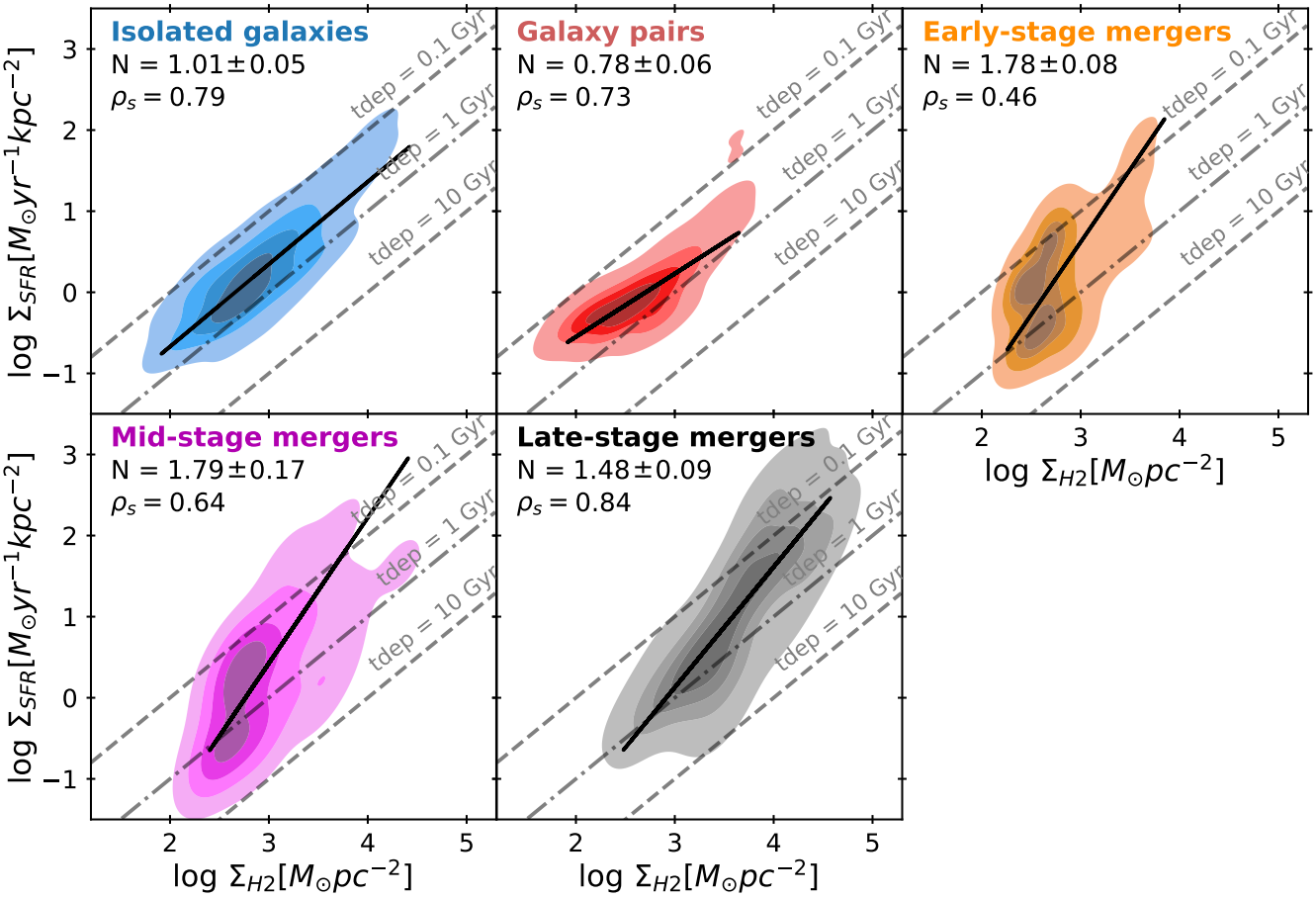

Fig. 7: KS diagram as a function of galaxy merger stage based on clump identification. From left to right and top to bottom, the merger stages are: isolated galaxies (blue), galaxy pairs (red), early-stage mergers (orange), mid-stage mergers (magenta) and late-stage mergers (black). The black solid line represents the best fit for each dataset. The Spearman's rank correlation coefficients (ρ_s) and the power-law indices (N) of the derived best-fit KS relations at the top-left of each panel. The grey dashed lines mark constant gas depletion times ($t_{dep} = \Sigma_{H2}/\Sigma_{SFR}$).

Table 3: Statistical parameters of the KS diagram across the merger sequence for clumps and beam-sized regions

Merger	Clumps				Beam-sized regions			
stages	ρ_s	$\log_{10}\frac{\Sigma_{H2}}{M_\odot pc^{-2}}$	$\log_{10}\frac{\Sigma_{SFR}}{M_\odot yr^{-1}kpc^{-2}}$	Slope	ρ_s	$\log_{10}\frac{\Sigma_{H2}}{M_\odot pc^{-2}}$	$\log_{10}\frac{\Sigma_{SFR}}{M_\odot yr^{-1}kpc^{-2}}$	Slope
Isolated	0.79	2.89 ± 0.38	0.25 ± 0.43	1.01 ± 0.05	0.70	3.33 ± 0.37	0.64 ± 0.47	0.92 ± 0.03
Pairs	0.73	2.64 ± 0.34	-0.03 ± 0.32	0.78 ± 0.06	0.73	2.85 ± 0.27	0.22 ± 0.35	1.05 ± 0.04
Early-stage	0.46	2.73 ± 0.24	0.11 ± 0.49	1.78 ± 0.08	0.64	3.20 ± 0.31	0.51 ± 0.52	1.09 ± 0.03
Mid-stage	0.64	2.93 ± 0.34	0.22 ± 0.59	1.79 ± 0.17	0.69	3.23 ± 0.33	0.33 ± 0.55	1.08 ± 0.04
Late-stage	0.84	3.62 ± 0.41	1.05 ± 0.76	1.48 ± 0.09	0.85	3.57 ± 0.45	0.94 ± 0.65	1.05 ± 0.02

Notes. For each merger stage (isolated galaxies, galaxy pairs, early-stage mergers, mid-stage mergers, and late-stage mergers), the table lists the Spearman's rank correlation coefficient ρ_{sp} (two-sided p-values), the mean and error bars (from the mean absolute deviation) of $\log_{10}\Sigma_{H2}$ $[M_\odot pc^{-2}]$ and $\log_{10}\Sigma_{SFR}$ $[M_\odot yr^{-1}kpc^{-2}]$, and the best-fit power-law indices. The slope of the KS law, when using clump identification, becomes super-linear in early and more advanced stage mergers, indicating larger star formation efficiencies at higher gas surface densities.

formation process, leading to variations in velocity dispersion, gas boundedness, and efficiency.

4.3. Radial distribution of the physical properties of clumps as a function of the merger stage

In this section, we analyse the variation of the gas clump properties as a function of their projected distance to the galaxy nuclei and also as a function of the effective radius of the clumps. To do so, we only use the results obtained through the clump method, and focus on individual clump SFRs, molecular masses, SFEs, velocity dispersions and their self-gravity (see Figures 11 and 12).

When examining the results as a function of merger stages in Figure 11, we find that the SFR of individual clumps decreases with increasing galactocentric radius, while the mass of the clumps remains generally constant, leading to a decrease in SFE at larger radii. Late-stage mergers show more massive

Table 4: Statistical parameters of the t_{dep} vs. b relation across the merger sequence for clumps and beam-sized regions.

Merger stages	Clumps				Beam-sized regions			
	ρ_s	$\log_{10}\frac{b}{M_\odot pc^{-2}(kms^{-1})^{-2}}$	$\log_{10}\frac{t_{dep}}{Myr}$	slope	ρ_s	$\log_{10}\frac{b}{M_\odot pc^{-2}(kms^{-1})^{-2}}$	$\log_{10}\frac{t_{dep}}{Myr}$	slope
Isolated galaxies	-0.06	-0.24 ± 0.58	2.64 ± 0.25	-0.01 ± 0.01	-0.20	0.46 ± 0.32	2.93 ± 0.32	-0.21 ± 0.01
Galaxy pairs	0.35	-0.57 ± 0.40	2.67 ± 0.21	0.18 ± 0.01	0.02	-0.07 ± 0.20	2.81 ± 0.22	0.02 ± 0.01
Early-stage	0.12	-1.22 ± 0.46	2.61 ± 0.41	0.24 ± 0.03 / -0.87 ± 0.01	-0.19	0.33 ± 0.30	2.97 ± 0.41	-0.33 ± 0.05
Mid-stage	-0.44	-0.72 ± 0.61	2.72 ± 0.46	-0.67 ± 0.11	-0.27	0.05 ± 0.26	3.21 ± 0.35	-0.41 ± 0.03
Late-stage	-0.61	0.47 ± 0.36	-2.57 ± 0.41	-0.66 ± 0.05	0.10	0.59 ± 0.44	3.09 ± 0.30	0.09 ± 0.01

Notes. For each merger stage (isolated galaxies, galaxy pairs, early-stage mergers, mid-stage mergers, and late-stage mergers), the table lists the Spearman's rank correlation coefficient ρ_{sp} (two-sided p-values), the mean and error bars (from the mean absolute deviation) of $\log_{10}b$ [$M_\odot pc^2$(km s^{-1})$^{-2}$] and $\log_{10}t_{dep}$ [Myr], and the best-fit power-law indices (slopes). For early-stage mergers we use MARS fit.

Table 5: Statistical parameters of the SFE vs. σ relation across the merger sequence for clumps and beam-sized regions.

Merger stages	Clumps			Beam-sized regions		
	ρ_s	$\frac{\sigma}{kms^{-1}}$	$\log_{10}\frac{SFE}{Myr^{-1}}$	ρ_s	$\frac{\sigma}{kms^{-1}}$	$\log_{10}\frac{SFE}{Myr^{-1}}$
Isolated galaxies	-0.08	44.00 ± 21.11	-2.64 ± 0.25	-0.43	27.72 ± 13.57	-2.93 ± 0.32
Galaxy pairs	0.06	45.84 ± 18.71	-2.67 ± 0.21	-0.39	28.78 ± 10.12	-2.81 ± 0.22
Early-stage	0.13	103.50 ± 32.37	-2.61 ± 0.41	-0.30	31.13 ± 13.27	-2.97 ± 0.41
Mid-stage	-0.68	76.83 ± 34.43	-2.72 ± 0.46	-0.28	43.21 ± 14.40	-3.21 ± 0.35
Late-stage	-0.10	40.93 ± 13.42	2.57 ± 0.41	-0.18	34.58 ± 12.43	-3.09 ± 0.30

Notes. For each merger stage (isolated galaxies, galaxy pairs, early-stage mergers, mid-stage mergers, and late-stage mergers), the table lists the Spearman's rank correlation coefficient ρ_{sp} (two-sided p-values), the mean and error bars (from the mean absolute deviation) of σ [km s^{-1}] and $\log_{10}$ SFE [Myr^{-1}].

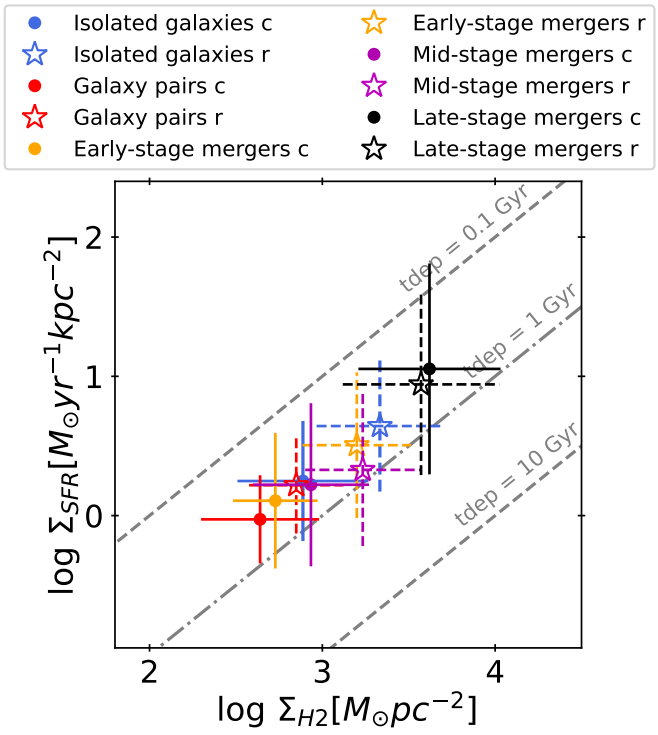

Fig. 8: The mean values of the KS diagram for each merger stage using both methodologies: open stars for beam-sized regions method and dots for the clumps method. The error bars indicate the mean absolute deviation.

clumps and higher median SFR. The self-gravity of the gas decreases with the radius in the different merger stages, except in late-stage mergers which is roughly constant and with higher values compared to the rest of merger stages. The velocity dispersion of the clumps tends to increase with the galactocentric radius. Within the central 2 kpc, the velocity dispersion decreases with galactocentric radius, but it increases again at larger radius. It is interesting to note the spatial distribution of the clumps; in particular, clumps in late-stage mergers are predominantly located at small galactocentric radius from the galaxies nuclei, confirming that most of the activity is concentrated in the central regions.

When we study the relation of the size of the clumps with the different parameters (see Figure 12), we find that the SFR increases with the size of the clumps, while the SFE remains approximately constant. The self-gravity of the clumps is approximately constant. The velocity dispersion of the gas increases with the size of the clumps in galaxy pairs, mid-stage and late-stage merger. The other merger stages show a constant trend.

Observations of molecular clouds in our Galaxy and a number of nearby galaxies have identified various empirical trends manifesting such cloud–environment correlations. Within a galaxy, molecular clouds located closer to the galaxy centre appear denser, more massive, and more turbulent (e.g. Oka et al. 2001; Colombo et al. 2014; Freeman et al. 2017; Hirota et al. 2018; Brunetti et al. 2021). An exception to this trend is observed in the early-stage LIRG NGC 5258 (Arp 240), where the brightest clumps are entirely extranuclear (Saravia et al. 2025). In our sample, we find more massive clumps and with higher SFR in late-stage mergers.

5. Summary and Conclusions

We have presented a spatially resolved study of the star formation relations in a sample of 27 local LIRGs, on scales of ~ 90 pc, spanning the entire merger sequence, from isolated to late stage mergers. We combined HST Paα and Paβ emission with ALMA CO(2–1) data to determine the SFR and molecular gas content in our galaxy sample. We have also investigated the potential influence of the merger process on the star formation in our sam-

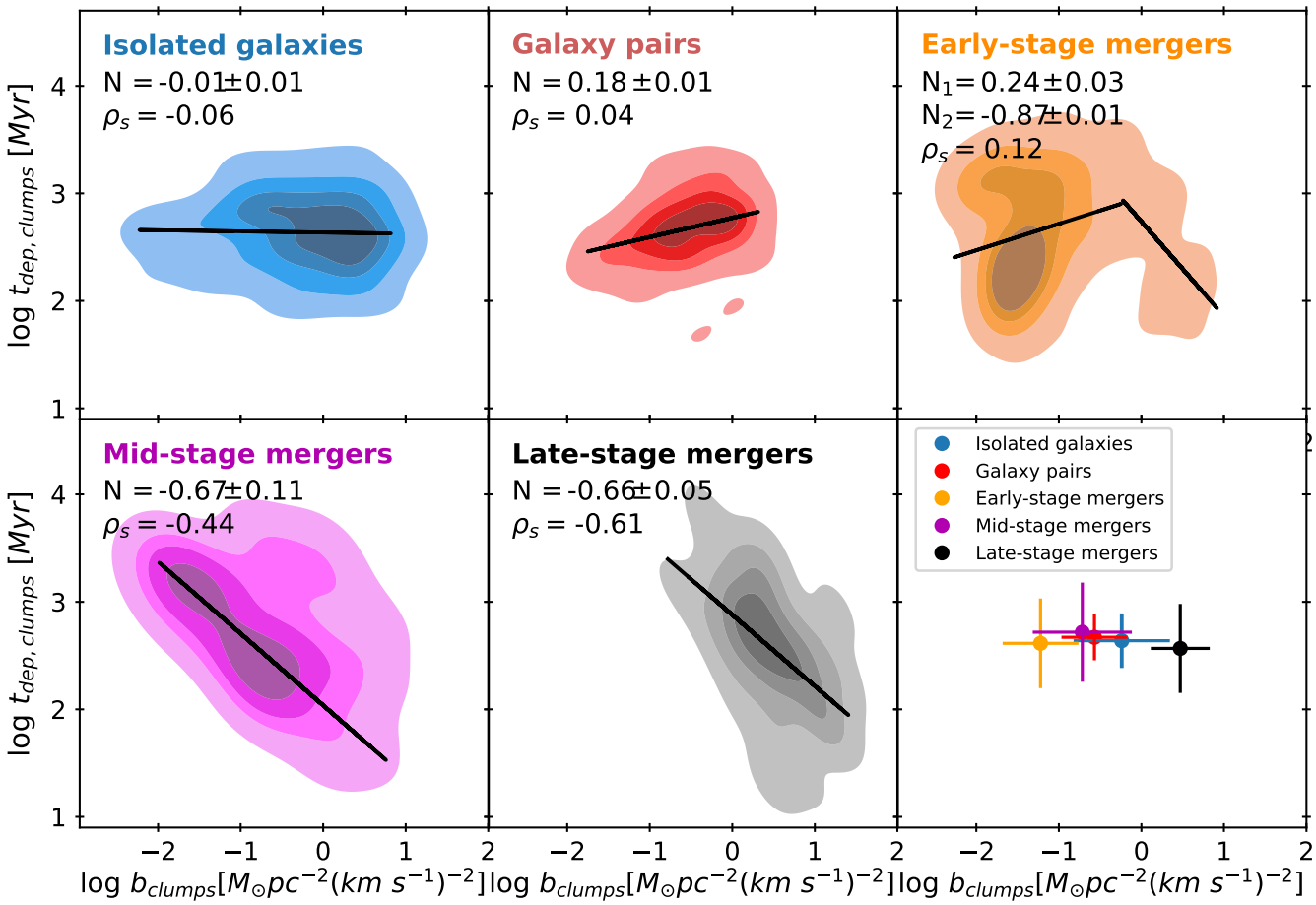

Fig. 9: Cold molecular gas depletion time, $t_{\rm dep,clumps}$, as a function of the self-gravity of the clumps (parameter b_{clumps}) across the merger sequence. From left to right and top to bottom, the merger stages are: isolated (blue), pair (red) of galaxies, early-stage mergers (orange), mid-stage mergers (magenta) and late-stage mergers (black). The Spearman's rank correlation coefficients (ρ_s) and the power-law indices (N) of the best-fit relations are indicated. The bottom right panel shows the mean values of $log_{10}t_{dep,clumps}$ and $log_{10}b_{clumps}$ for each merger stage. The error bars indicate the mean absolute deviation. The slope of the correlation between$t_{dep,clumps}$ and b_{clumps} transitions from relatively flat, to a broken power law at early merger stages, to a negative slope in mid- and late-stage mergers, indicating the most bounded gas clumps are depleting their gas reservoir faster at the latest stages of the interaction.

ple, measuring the depletion time, star formation efficiency, as well as the self-gravity of the gas and velocity dispersion of the gas. We used two different methods: 1) sampling the emission of the galaxies with beam-sized regions, and 2) identifying physical structures (clumps) using the identification algorithm Astrodendro.

The main results of this paper are summarized as follows:

- We derived spatially resolved KS relations for each LIRG of the sample, using beam-sized regions and clumps. When using beam-size regions, we identified two different behaviours in the KS plot using the regions selection: 67% of galaxies follow a single trend, while the remain display two branches, suggesting the existence of a duality in this relation. However, when analysing physical clumps, the duality disappears, and only one single trend is observed.
- The two methods reveal variations in both the slope and the correlation coefficient. These results provide two different perspectives for studying the star formation relation: one focusing the statistics of gas and SF properties at the smallest scales, and the other targeting physically coherent gas clumps and structures.
- We studied galaxies according to its merger stage. We find the slope of the KS relation to become steeper as the merger progresses, reflecting changes in the SF efficiency of molecular gas clumps. In late-stage mergers, we observe higher values of Σ_{SFR} and Σ_{H2} compared to the other stages. However, when analysing the KS relation using beam-sized regions, the slopes remain close to one, displaying more homogeneous behaviour across the merger sequence.
- In isolated galaxies and up to early stage mergers, the gas depletion time of the clumps, $t_{dep,clumps}$, does not depend on their self-gravity, b_{clumps}. However, in later merger stages, clumps with higher self-gravity become more efficient at forming stars, exhibiting shorter gas depletion timescales.
- In early- and mid-stage mergers, the clumps exhibit higher velocity dispersion compared to the other stages of the merger sequence. However, clumps in early-stage mergers exhibit higher velocity dispersion but they are not very efficient. In late-stage mergers, the velocity dispersion of the gas shows a smaller range of values.
- The SFR of individual clumps decreases with increasing galactocentric radius, where 70% of the SFR in concentrated in the central 2.5 kpc, while the mass of the clumps

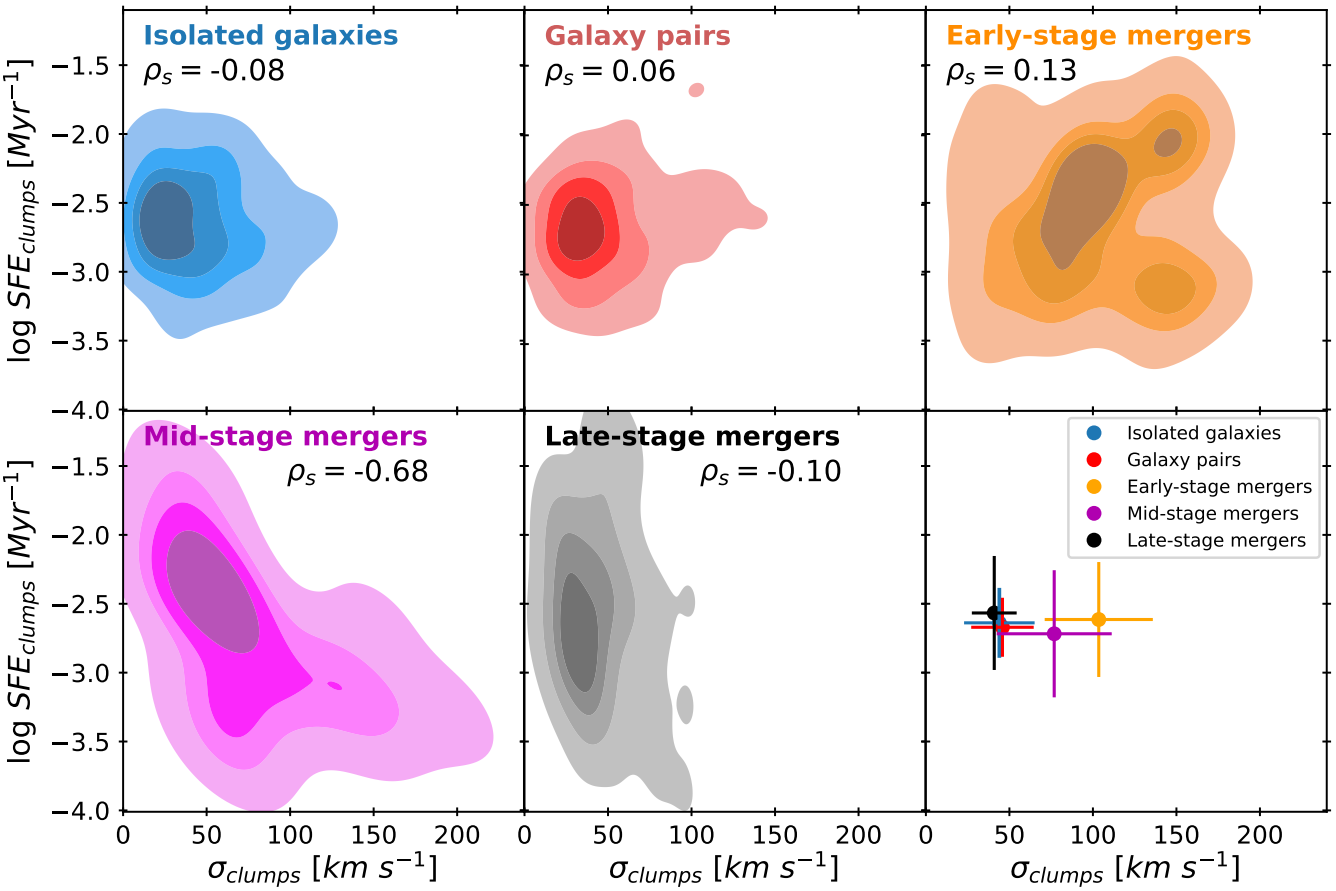

Fig. 10: SF efficiency as a function of the velocity dispersion of the clumps (σ_{clumps}) across the merger sequence. From left to right and top to bottom, the merger stages are: isolated galaxies (blue), galaxy pairs (red), early-stage mergers (orange), mid-stage mergers (magenta) and late-stage mergers (black). The Spearman's rank correlation coefficients (ρ_s) are indicated. The bottom right panel shows the mean values of the σ_{clumps} and $log_{10}SFE_{clumps}$ for each merger stage. The bottom right panel shows the mean valyes of $\log_{10}SFE_{clumps}$ and σ_{clumps} for each merger stage, with error bars representing the mean absolute deviation.

remains generally constant with the radius. Clumps in late-stage mergers tend to be more massive. The velocity dispersion of the clumps tend to decrease as a function of galactocentric radius within the inner ~2 kiloparsecs, but increases again at larger radii. The self-gravity of the gas decreases with radius across the different merger stages, except in late-stage mergers, where it remains approximately constant.

– We also find that the SFR increases with the size of the clumps, while the SFE remains approximately constant. Additionally, the velocity dispersion of the gas increases with the size of the clumps in pairs of galaxies, mid-stage, and late-stage mergers.

Acknowledgements. MSG acknowledges that this research project was supported by the Hellenic Foundation for Research and Innovation (HFRI) under the "2nd Call for HFRI Research Projects to support Faculty Members & Researchers" (Project Number: 03382). MSG also acknowledges support from the National Radio Astronomy Observatory Visitor Program. MSG and YS acknowledge support from the Joint ALMA Observatory Visitor Program. MPS acknowledges support under grants RYC2021-033094-I, CNS2023-145506 and PID2023-146667NB-I00 funded by MCIN/AEI/10.13039/501100011033 and the European Union NextGenerationEU/PRTR. CR acknowledges support from Fondecyt Regular grant 1230345, ANID BASAL project FB210003 and the China-Chile joint research fund. This research made use of Astrodendro, a Python package for computing dendrograms of astronomical data (http://www.dendrograms.org/). This paper makes use of the following ALMA data: ADS/JAO.ALMA#2013.1.00243.S, ADS/JAO.ALMA#2013.1.00271.S, ADS/JAO.ALMA#2015.1.00714.S, ADS/JAO.ALMA#2017.1.00255.S, ADS/JAO.ALMA#2017.1.00395.S. ALMA is a partnership of ESO (representing its member states), NSF (USA) and NINS (Japan), together with NRC (Canada), NSTC and ASIAA (Taiwan), and KASI (Republic of Korea), in cooperation with the Republic of Chile. The Joint ALMA Observatory is operated by ESO, AUI/NRAO and NAOJ.

References

Accurso, G., Saintonge, A., Catinella, B., et al. 2017, MNRAS, 470, 4750
Albrecht, M., Krügel, E., & Chini, R. 2007, A&A, 462, 575
Alonso-Herrero, A., Pereira-Santaella, M., Rieke, G. H., & Rigopoulou, D. 2012, ApJ, 744, 2
Alonso-Herrero, A., Rieke, G. H., Rieke, M. J., et al. 2006, ApJ, 650, 835
Armus, L., Heckman, T. M., & Miley, G. K. 1989, The Astrophysical Journal, 347, 741
Armus, L., Mazzarella, J. M., Evans, A. S., et al. 2009, PASP, 121, 559
Bellocchi, E., Pereira-Santaella, M., Colina, L., et al. 2022, A&A, 664, A60
Boggs, P. T., Byrd, R. H., & Schnabel, R. B. 1987, SIAM Journal on Scientific and Statistical Computing, 8, 1052
Böker, T., Calzetti, D., Sparks, W., et al. 1999, ApJS, 124, 95
Bolatto, A. D., Leroy, A. K., Rosolowsky, E., Walter, F., & Blitz, L. 2008, ApJ, 686, 948
Bolatto, A. D., Wolfire, M., & Leroy, A. K. 2013, ARA&A, 51, 207
Bonne, L., Kabanovic, S., Schneider, N., et al. 2023, A&A, 679, L5
Briggs, D. S. 1995, in American Astronomical Society Meeting Abstracts, Vol. 187, American Astronomical Society Meeting Abstracts, 112.02
Brunetti, N., Wilson, C. D., Sliwa, K., et al. 2021, MNRAS, 500, 4730
Chevance, M., Kruijssen, J. M. D., Hygate, A. P. S., et al. 2020, MNRAS, 493, 2872

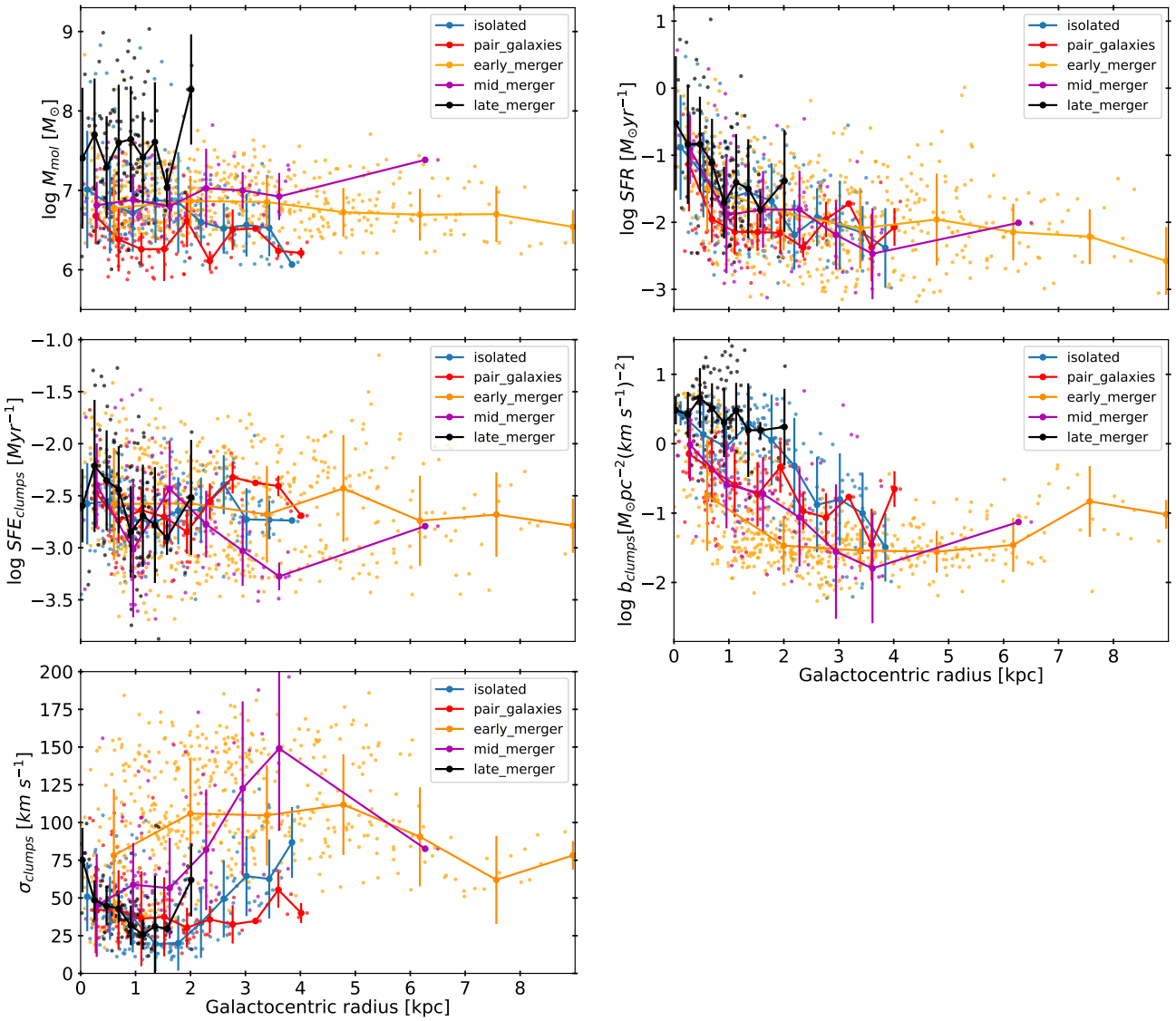

Fig. 11: Molecular gas mass (top left), SFR (top right), SFE (middle left), boundedness of the gas (middle right), velocity dispersion (bottom left) and effective radius of clumps as function of galactocentric radius across the sample. The data points show the median M_{mol}, SFR, SFE, b, σ and effective radius in bins of galactocentric distance for each merger stage. The error bars indicate the mean absolute deviation of the points in the bins.

Chevance, M., Kruijssen, J. M. D., Krumholz, M. R., et al. 2022, MNRAS, 509, 272
Choi, W., Liu, L., Bureau, M., et al. 2023, MNRAS, 522, 4078
Colombo, D., Hughes, A., Schinnerer, E., et al. 2014, ApJ, 784, 3
Corbelli, E., Braine, J., Bandiera, R., et al. 2017, A&A, 601, A146
Corbett, E. A., Kewley, L., Appleton, P. N., et al. 2003, ApJ, 583, 670
Daddi, E., Elbaz, D., Walter, F., et al. 2010, ApJ, 714, L118
Demachi, F., Fukui, Y., Yamada, R. I., et al. 2024, PASJ, 76, 1059
Díaz-Santos, T., Armus, L., Charmandaris, V., et al. 2017, ApJ, 846, 32
Downes, D. & Solomon, P. M. 1998, ApJ, 507, 615
Federrath, C. & Klessen, R. S. 2013, ApJ, 763, 51
Freeman, P., Rosolowsky, E., Kruijssen, J. M. D., Bastian, N., & Adamo, A. 2017, MNRAS, 468, 1769
Friedman, J. H. 1991, The Annals of Statistics, 19, 1
Fukui, Y. & Kawamura, A. 2010, ARA&A, 48, 547
Garay, G., Mardones, D., & Mirabel, I. F. 1993, A&A, 277, 405
García-Burillo, S., Usero, A., Alonso-Herrero, A., et al. 2012, A&A, 539, A8
García-Marín, M., Colina, L., & Arribas, S. 2009, AA, 505, 1017
Genzel, R., Tacconi, L. J., Gracia-Carpio, J., et al. 2010, MNRAS, 407, 2091
Grudić, M. Y., Hafen, Z., Rodriguez, C. L., et al. 2022, Monthly Notices of the Royal Astronomical Society, 519, 1366
Hennebelle, P. & Chabrier, G. 2011, ApJ, 743, L29
Herrero-Illana, R., Privon, G. C., Evans, A. S., et al. 2019, A&A, 628, A71
Heyer, M. & Dame, T. M. 2015, ARA&A, 53, 583
Hirota, A., Egusa, F., Baba, J., et al. 2018, PASJ, 70, 73
Hopkins, P. F., Somerville, R. S., Hernquist, L., et al. 2006, ApJ, 652, 864
Iono, D., Yun, M. S., & Ho, P. T. P. 2005, ApJS, 158, 1
Jeffreson, S. M. R., Kruijssen, J. M. D., Keller, B. W., Chevance, M., & Glover, S. C. O. 2020, MNRAS, 498, 385
Kennicutt, Robert C., J. 1998, ARA&A, 36, 189
Kennicutt, R. C. & Evans, N. J. 2012, ARA&A, 50, 531
Kewley, L. J., Dopita, M. A., Sutherland, R. S., Heisler, C. A., & Trevena, J. 2001, ApJ, 556, 121
Kim, J., Chevance, M., Kruijssen, J. M. D., et al. 2022, MNRAS, 516, 3006
Kreckel, K., Faesi, C., Kruijssen, J. M. D., et al. 2018, ApJ, 863, L21
Kroupa, P. 2001, MNRAS, 322, 231
Kruijssen, J. M. D. & Longmore, S. N. 2014, MNRAS, 439, 3239
Krumholz, M. R. & McKee, C. F. 2005, ApJ, 630, 250
Larson, K. L., Díaz-Santos, T., Armus, L., et al. 2020, ApJ, 888, 92
Larson, K. L., Sanders, D. B., Barnes, J. E., et al. 2016, The Astrophysical Journal, 825, 128
Leroy, A. K., Hughes, A., Schruba, A., et al. 2016, ApJ, 831, 16
Leroy, A. K., Schinnerer, E., Hughes, A., et al. 2017, ApJ, 846, 71
Leroy, A. K., Schinnerer, E., Hughes, A., et al. 2021, ApJS, 257, 43
Leroy, A. K., Walter, F., Martini, P., et al. 2015, ApJ, 814, 83
Li, H., Vogelsberger, M., Bryan, G. L., et al. 2022, MNRAS, 514, 265

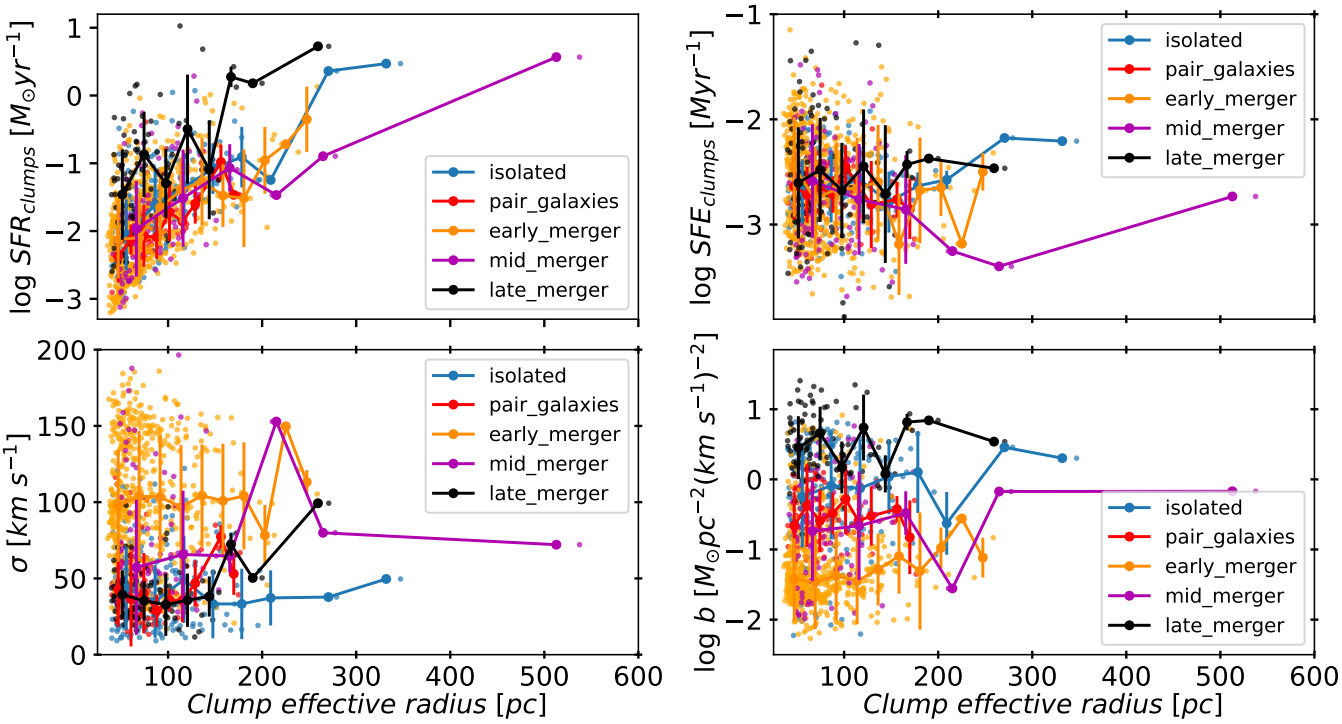

Fig. 12: SFR (top left), SFE (top right), velocity dispersion (bottom left) and self-gravity of the clumps as function of clump sizes. The circles show the median SFR, SFE, σ and b in bins of clump sizes for each merger stage. The error bars indicate the mean absolute deviation of the points in the bins.

Liu, L., Bureau, M., Li, G.-X., et al. 2022, MNRAS, 517, 632
McMullin, J. P., Waters, B., Schiebel, D., Young, W., & Golap, K. 2007, in Astronomical Society of the Pacific Conference Series, Vol. 376, Astronomical Data Analysis Software and Systems XVI, ed. R. A. Shaw, F. Hill, & D. J. Bell, 127
Miville-Deschênes, M.-A., Murray, N., & Lee, E. J. 2017, ApJ, 834, 57
Montoya Arroyave, I., Cicone, C., Makroleivaditi, E., et al. 2023, A&A, 673, A13
Oey, M. S., Parker, J. S., Mikles, V. J., & Zhang, X. 2003, AJ, 126, 2317
Oka, T., Hasegawa, T., Sato, F., et al. 2001, ApJ, 562, 348
Orkisz, J. H., Pety, J., Gerin, M., et al. 2017, A&A, 599, A99
Osterbrock, D. E. & Ferland, G. J. 2006, Astrophysics of gaseous nebulae and active galactic nuclei
Papadopoulos, P. P., van der Werf, P., Xilouris, E., Isaak, K. G., & Gao, Y. 2012, ApJ, 751, 10
Pereira-Santaella, M., Alonso-Herrero, A., Santos-Lleo, M., et al. 2011, A&A, 535, A93
Pereira-Santaella, M., Colina, L., García-Burillo, S., et al. 2016a, A&A, 594, A81
Pereira-Santaella, M., Colina, L., García-Burillo, S., et al. 2021, A&A, 651, A42
Pereira-Santaella, M., Colina, L., García-Burillo, S., et al. 2016b, A&A, 587, A44
Pereira-Santaella, M., Diamond-Stanic, A. M., Alonso-Herrero, A., & Rieke, G. H. 2010, ApJ, 725, 2270
Pessa, I., Schinnerer, E., Belfiore, F., et al. 2021, A&A, 650, A134
Piqueras López, J., Colina, L., Arribas, S., & Alonso-Herrero, A. 2013, A&A, 553, A85
Rey-Raposo, R., Dobbs, C., Agertz, O., & Alig, C. 2017, MNRAS, 464, 3536
Ricci, C., Privon, G. C., Pfeifle, R. W., et al. 2021, MNRAS, 506, 5935
Rich, J. A., Torrey, P., Kewley, L. J., Dopita, M. A., & Rupke, D. S. N. 2012, ApJ, 753, 5
Rodríguez-Zaurín, J., Arribas, S., Monreal-Ibero, A., et al. 2011, A&A, 527, A60
Rosolowsky, E. W., Pineda, J. E., Kauffmann, J., & Goodman, A. A. 2008, ApJ, 679, 1338
Saito, T., Iono, D., Xu, C. K., et al. 2017, ApJ, 835, 174
Sánchez, S. F., Rosales-Ortega, F. F., Iglesias-Páramo, J., et al. 2014, A&A, 563, A49
Sánchez-García, M., García-Burillo, S., Pereira-Santaella, M., et al. 2022b, Astronomy Astrophysics, 660, A83
Sánchez-García, M., Pereira-Santaella, M., García-Burillo, S., et al. 2022a, A&A, 659, A102
Sanders, D. B., Mazzarella, J. M., Kim, D. C., Surace, J. A., & Soifer, B. T. 2003, AJ, 126, 1607
Sanders, D. B. & Mirabel, I. F. 1996, Annual Review of Astronomy and Astrophysics, 34, 749
Saravia, A., Rodas-Quito, E., Barcos-Muñoz, L., et al. 2025, ApJ, 979, 217
Schinnerer, E. & Leroy, A. K. 2024, ARA&A, 62, 369
Schmidt, M. 1959, ApJ, 129, 243
Schruba, A., Kruijssen, J. M. D., & Leroy, A. K. 2019, ApJ, 883, 2
Stierwalt, S., Armus, L., Surace, J. A., et al. 2013, ApJS, 206, 1
Sun, J., Leroy, A. K., Rosolowsky, E., et al. 2022, AJ, 164, 43
Sun, J., Leroy, A. K., Schinnerer, E., et al. 2020, ApJ, 901, L8
Sun, J., Leroy, A. K., Schruba, A., et al. 2018, ApJ, 860, 172
Teng, Y.-H., Chiang, I.-D., Sandstrom, K. M., et al. 2024, ApJ, 961, 42
Teng, Y.-H., Sandstrom, K. M., Sun, J., et al. 2023, ApJ, 950, 119
Utomo, D., Sun, J., Leroy, A. K., et al. 2018, ApJ, 861, L18
Veilleux, S., Kim, D. C., Sanders, D. B., Mazzarella, J. M., & Soifer, B. T. 1995, ApJS, 98, 171
Yuan, T. T., Kewley, L. J., & Sanders, D. B. 2010, ApJ, 709, 884
Zetterlund, E., Glenn, J., & Rosolowsky, E. 2019, ApJ, 881, 90

[1] Institute of Astrophysics, Foundation for Research and Technology-Hellas (FORTH), Heraklion, 70013, Greece
e-mail: msanchez@ia.forth.gr
[2] Department of Physics, University of Crete, Heraklion, 71003, Greece
[3] National Radio Astronomy Observatory, 520 Edgemont Road, Charlottesville, VA 22903, USA
[4] Department of Astronomy, University of Virginia, 530 McCormick Road, Charlottesville, VA 22903, USA
[5] European Southern Observatory, Alonso de Córdova, 3107, Vitacura, Santiago 763-0355, Chile
[6] Joint ALMA Observatory, Alonso de Córdova, 3107, Vitacura, Santiago 763-0355, Chile
[7] Instituto de Física Fundamental, CSIC, Calle Serrano 123, 28006 Madrid, Spain
[8] Observatorio Astronómico Nacional (OAN-IGN)-Observatorio de Madrid, Alfonso XII, 3, 28014 Madrid, Spain

[9] Steward Observatory, University of Arizona, 933 N Cherry Avenue, Tucson, AZ 85721, USA
[10] Instituto de Estudios Astrofísicos, Facultad de Ingeniería y Ciencias, Universidad Diego Portales, Av. Ejército Libertador 441, Santiago, Chile
[11] IPAC, California Institute of Technology, 1200 E. California Blvd., Pasadena, CA 91125, USA
[12] INAF – Osservatorio di Astrofisica e Scienza dello Spazio di Bologna, Via Gobetti 93/3, 40129, Bologna, Italy
[13] Department of Astronomy, University of Maryland, 4296 Stadium Drive, College Park, MD 20742, USA
[14] Leiden Observatory, Leiden University, PO Box 9513, 2300 RA Leiden, The Netherlands
[15] Department of Astronomy, University of Florida, 1772 Stadium Road, Gainesville, FL 32611, USA
[16] Faculty of Global Interdisciplinary Science and Innovation, Shizuoka University, 836 Ohya, Suruga-ku, Shizuoka 422-8529, Japan
[17] AURA for the European Space Agency (ESA), Space Telescope Science Institute, 3700 San Martin Drive, Baltimore, MD 21218, USA
[18] Department of Physics and Astronomy, University of California, 4129 Frederick Reines Hall, Irvine, CA 92697, USA
[19] Department of Physics & Astronomy and Ritter Astrophysical Research Center, University of Toledo, Toledo, OH 43606,USA
[20] zz
[21] Ritter Astrophysical Research Center, University of Toledo, Toledo, OH 43606, USA
[22] Hiroshima Astrophysical Science Center, Hiroshima University, 1-3-1 Kagamiyama, Higashi-Hiroshima, Hiroshima 739-8526, Japan
[23] Universidad Nacional Autónoma de Honduras, Ciudad Universitaria, Tegucigalpa, Honduras

Appendix A: Comparison between one and two configurations in ALMA data

From our sample of 23 LIRG systems, 43% (10 systems) have observations using a single 12 m configuration. The remaining 57% (13 systems) were also studied in Sánchez-García et al. (2022a), where observations were conducted with two 12 m configurations (one more extended and one more compact). The use of only one extended configuration filters out spatial scales larger than those sampled by the shortest baselines. Additionally, it is well-known that flux is lost even before reaching the maximum recoverable scale (MRS).

We are interested in determining the properties of molecular gas at scales of ∼ 100 pc (∼0.2") in local LIRGs. This scale is smaller than the MRS, so the missing flux due to the absence of short spacing is expected to be minimal. However, we expect to lose flux at scales larger than ∼2.5" (∼ 1.2 kpc).

To evaluate the influence of using one or two configurations on clump detection, we compared the identified regions (clumps) in observations of IC 5179 using different configurations, as shown in Figure A.1.

We find that most of the clumps identified in the two-configuration observations are also detected in the single-configuration observations. This result suggests that the identification of clumps in observations with different configurations does not significantly impact the study of the star formation process in molecular clumps.

Appendix B: Comparison and effects of the selected CO-to-H_2 conversion factor

We used a fixed Galactic CO-to-H_2 conversion factor to estimate the molecular gas mass of our sample. However, this factor depends on the properties of the gas, including temperature, density, and metallicity. Its precise value remains a topic of debate and can vary significantly across different environments, particularly in extreme conditions such as those found in (U)LIRGs. Recent studies of star-forming regions within the PHANGS sample, at 90-150 pc scales, have revealed that the velocity dispersion of molecular gas significantly influences the value of α_{CO}. For instance, Teng et al. (2023, 2024) reported a strong anti-correlation between α_{CO} and the local cloud-scale velocity dispersion. Higher velocity dispersion enhances the rate of collisional excitation of molecules, potentially leading to an overestimation of α_{CO}.

The fitted function derived from a galaxy sample, using velocity dispersion measurements at a 90 pc scale (Teng et al. 2024) is as follows:

$$log_{10}\alpha_{co} = -0.59(\pm0.04)\ log < \sigma_{gas} >_{90pc} + 0.90(\pm0.03) \quad \text{(B.1)}$$

By applying the σ_{gas}-based α_{CO} prescription[8] to our sample, we aim to verify that this α_{CO} prescription does not alter the results of this work. We use two approaches: 1) we use α_{CO} values derived from the equation, and 2) we assume a fixed value in the regime where the velocity dispersion is not covered by Teng et al. (2024). This second approach is considered because the galaxies in our sample cover higher velocity dispersion values than the range explored in the PHANGS sample. The regime of high velocity dispersion values has not been explored in the σ_{gas}-based α_{CO} prescription, which makes the behaviour of the factor with velocity dispersion uncertain. The PHANGS sample covers values of velocity dispersion up to ∼35 km/s, whereas the galaxies in our sample exceed this range of values.

As an example, Fig. B.1 shows the KS plot for the galaxy NGC5135. We obtain similar results with the only difference of the lower values in the molecular gas surface density. For the case of dual galaxies, we still obtain the dual behaviour and the single power law for the galaxies using the clumps methodology. The only difference is in the range of values of the x-axis where the surface density of molecular gas is lower, with a shift of ∼ 0.55 dex. This implies that the depletion time changes by a factor of approximately 3.7. However, we can conclude that the different prescriptions for the conversion factor do not affect the main results of this work.

[8] Equation (B.1) follows the formulation from private communication and will be included in a forthcoming paper.

Appendix C: Figures

Appendix C.1: Spatial distribution of the dual behaviour in the KS diagram for the LIRG NGC 3110

In this Appendix, we show as an example the spatial locations of the regions in NGC 3110, which exhibits dual behaviour.

Appendix C.2: Star formation properties as a function of merger stage using beam-sized regions

we present the figures for the study of star-formation properties in the sample using the beam-sized region methodology. Figure C.2 shows the distribution of regions across merger stages; Figure C.3 presents the Kennicutt-Schmidt law; Figure C.4 displays the cold molecular-gas depletion time as a function of the self-gravity of the regions; and Figure C.5 shows the star-formation efficiency as a function of the velocity dispersion of the regions.

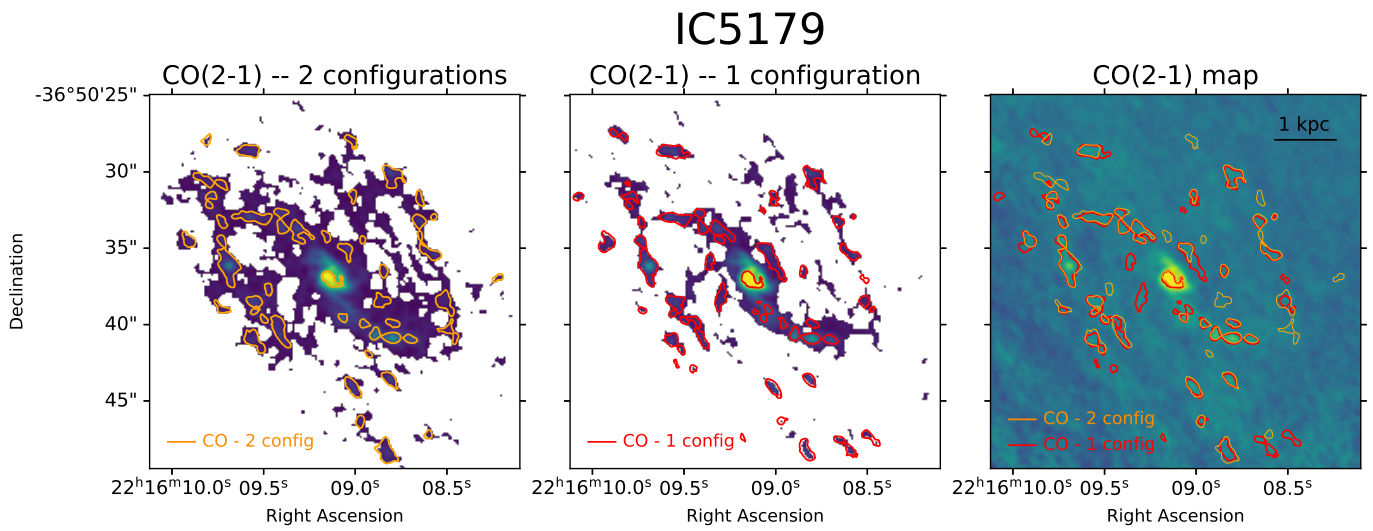

Fig. A.1: CO(2–1) integrated intensity maps of IC 5179 at 90 pc scales, obtained with ALMA using two configurations (*left panel*) and only one extended configuration (*middle panel*). These maps illustrate, with orange and red contours, the identified regions from the dendrogram analysis detailed in Sect. 3.1.2, applied to each map based in the same criteria. The map without clipping (*right panel*) displays the clumps identified in the maps. from observations using both one and two configurations.

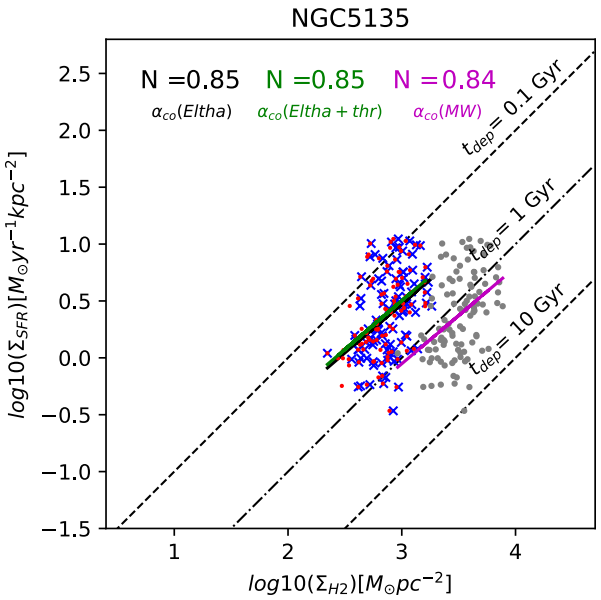

Fig. B.1: SFR surface density as a function of the molecular gas surface density at 90 pc in NGC5135 using three different prescriptions in the conversion factor: σ_{gas}-based α_{CO} prescription (black fit), the same prescription with a threshold in the region of velocity dispersion unexplored (green fit) and the galactic conversion factor (magenta fit).

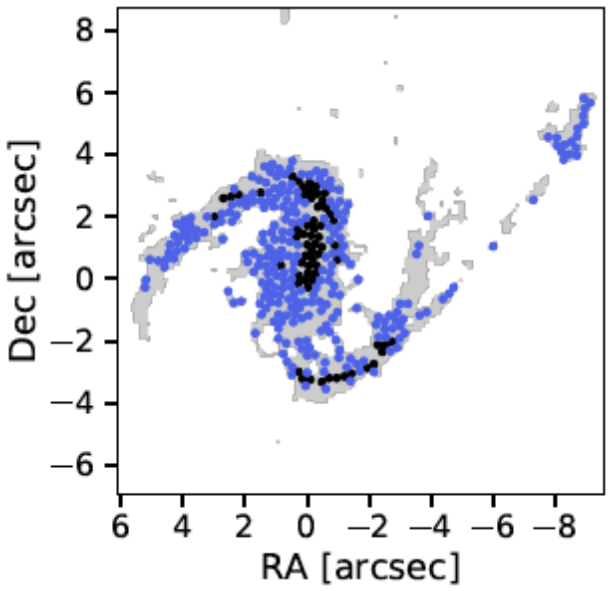

Fig. C.1: Location of the regions on the CO(2–1) map (grey) for NGC 3110. The black and blue circles correspond to regions in each of the two branches.

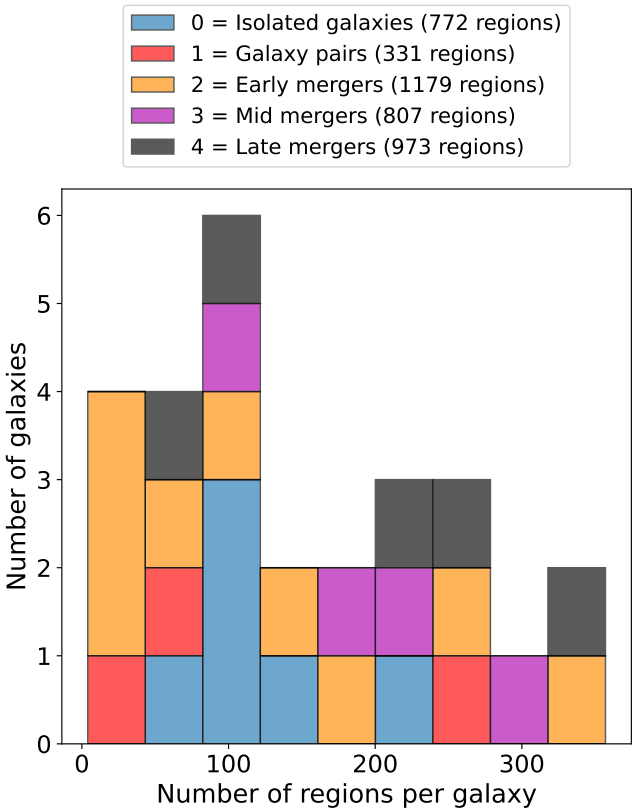

Fig. C.2: Distribution of the number of regions per galaxy across the different merger stages in the galaxy sample. The early-, mid-, and late-stage mergers cover the entire range of the stacked histogram, while isolated galaxies show lower number of regions per galaxy.

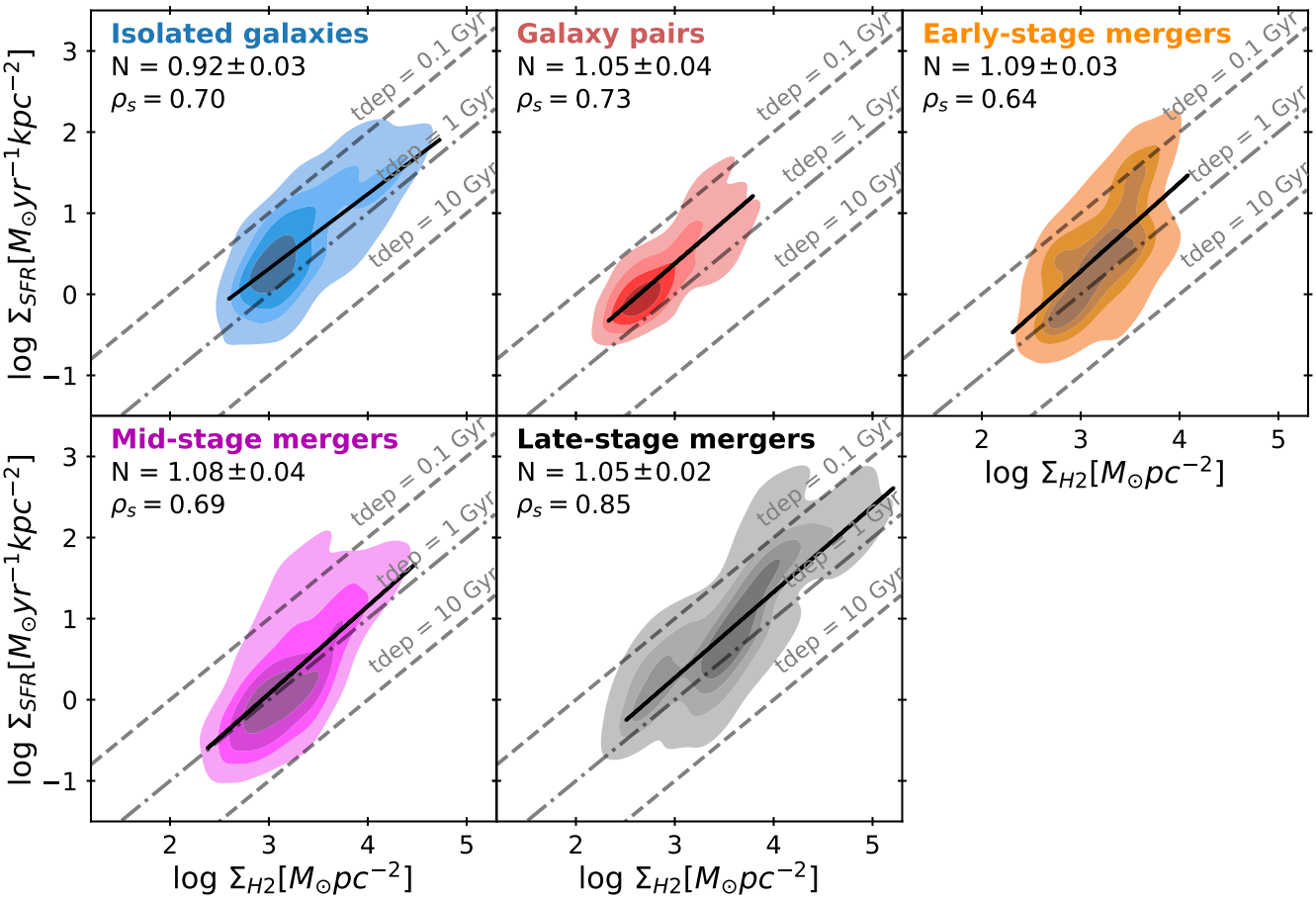

Fig. C.3: Representation of the KS diagram across the merger sequence based on beam-sized region identification. From left to right and top to bottom, the merger stages are: isolated galaxies (blue), galaxy pairs (red), early-stage mergers (orange), mid-stage mergers (magenta) and late-stage mergers (black). The black solid line represents the best fit for each dataset. The Spearman's rank correlation coefficients (ρ_s) and the power-law indices (N) of the derived best-fit KS relations are indicated. The bottom right panel shows the mean values of $\log_{10}\Sigma_{SFR}$ and $\log_{10}\Sigma_{H2}$, with error bars representing the mean absolute deviation for each merger stage. The grey dashed lines mark constant depletion times ($t_{dep} = \Sigma_{H2}/\Sigma_{SFR}$).

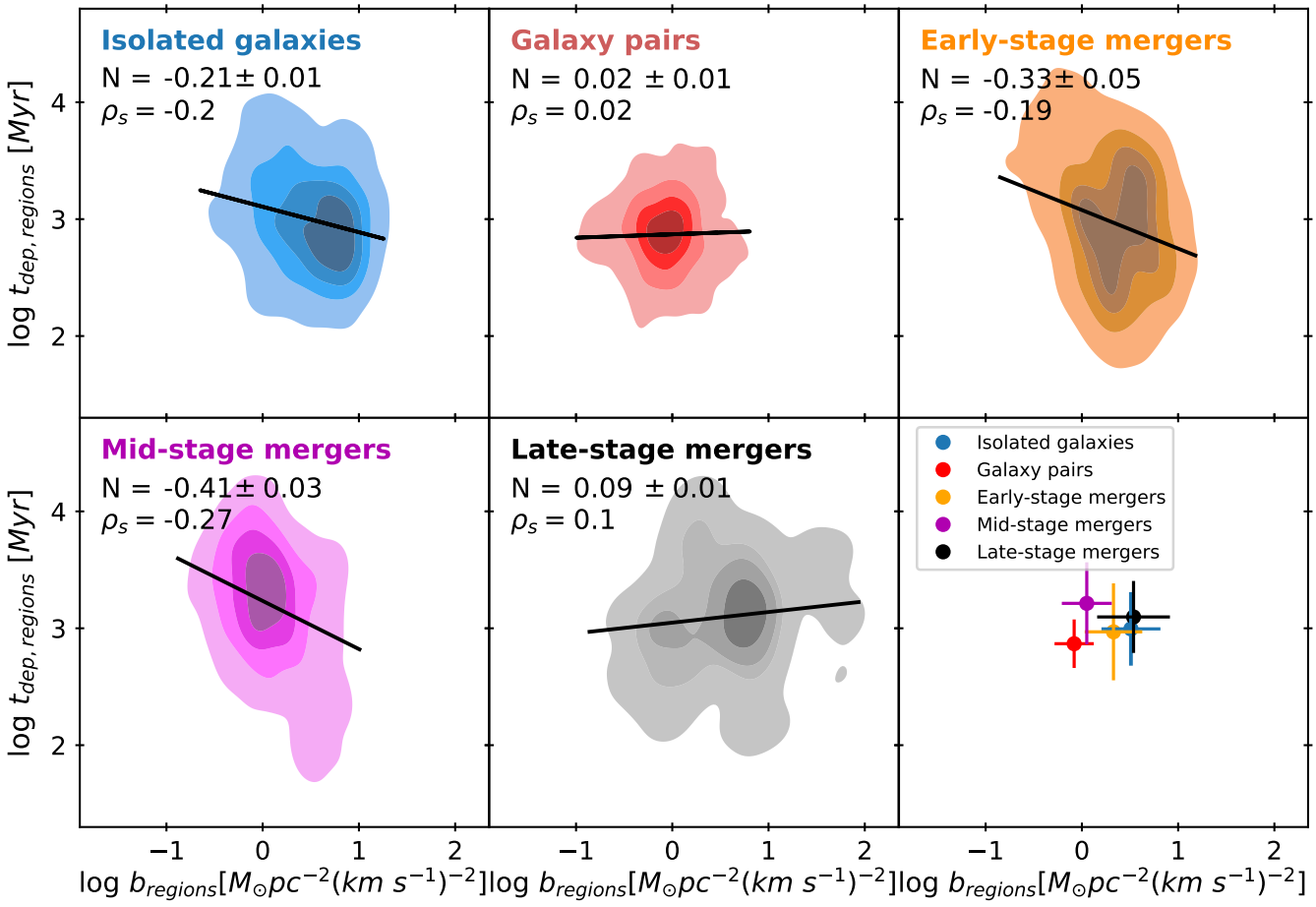

Fig. C.4: Cold molecular gas depletion time, t_{dep}, as a function of the self-gravity of the regions (parameter $b_{regions}$) across the merger sequence. From left to right and top to bottom, the merger stages are: isolated (blue), pair (red) of galaxies, early-stage mergers (orange), mid-stage mergers (magenta) and late-stage mergers (black). The Spearman's rank correlation coefficients (ρ_s) and the power-law indices (N) of the best-fit relations are indicated. The bottom right panel shows the mean values of $\log_{10} t_{dep}$ and $\log_{10} b_{regions}$, with error bars representing the mean absolute deviation for each merger stage.

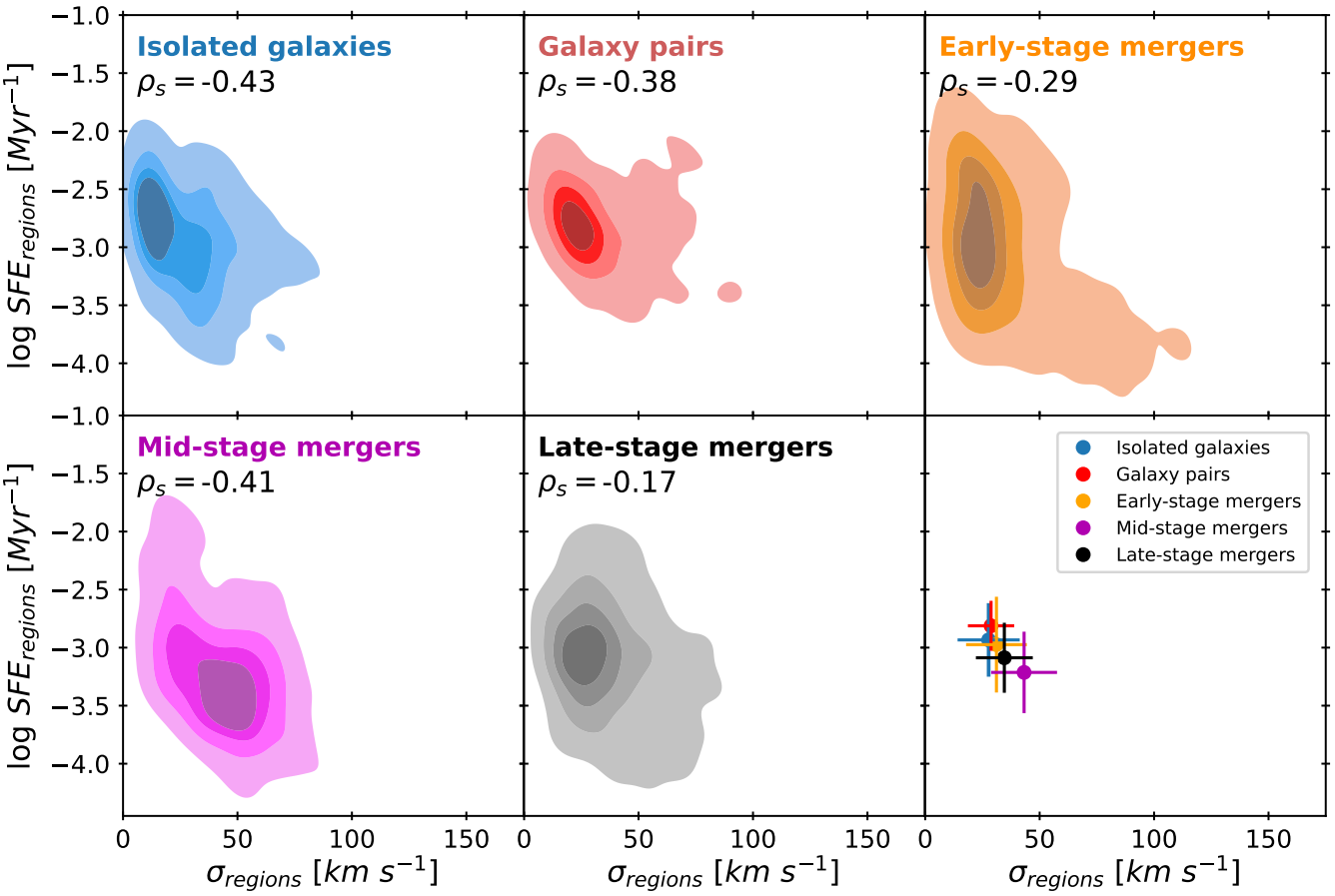

Fig. C.5: SF efficiency as a function of the velocity dispersion of the regions ($\sigma_{regions}$) across the merger sequence. From left to right and top to bottom, the merger stages are: isolated galaxies (blue), galaxy pairs (red), early-stage mergers (orange), mid-stage mergers (magenta) and late-stage mergers (black). The Spearman's rank correlation coefficients (ρ_s) are indicated. The bottom right panel shows the mean values of $\sigma_{regions}$ and $log_{10}SFE_{regions}$, with error bars representing the mean absolute deviation for each merger stage.